Part-Scale Build Orientation Optimization for Minimizing Residual Stress and Support Volume for Metal Additive Manufacturing: Theory and Experimental Validation

Lin Cheng[1] and Albert To[1*]

[1] Department of Mechanical Engineering and Materials Science, University of Pittsburgh, Pittsburgh, PA 15261

Abstract: Laser powder bed metal additive manufacturing (AM) has been widely accepted by the industry to manufacture end-use components with complex geometry to achieve desirable performance (i.e. conformal cooling). However, residual stress and large deformation introduced in the laser AM process leads to severe issues, such as cracks, delamination, and large deformation. These issues result in the stoppage of powder spreading and warpage of the component. To overcome these issues, a novel optimization framework based on fast process modeling is proposed to find the optimal build orientation by minimizing the maximum residual stress and support structure volume. For support generation, a voxel-based methodology is proposed to systematically capture support surfaces from STL file, form support structure, and generate Cartesian mesh for fast process modeling. Instead of using conformal mesh, the voxel-based fictitious domain method is used to calculate the stress distribution in the design domain including the support structure, which is represented by the homogenized model. This can circumvent time-consuming mesh generation for geometrically complex geometry and its support structure during the optimization iterations, thus making it possible to minimize residual stress through orientation optimization based on process modeling. Due to its self-supporting and open-cell nature, lattice structure is employed as the support structure to anchor the overhangs to the substrate to prevent distortion resulting from residual stress. Asymptotic homogenization (AH) method is employed to compute the effective properties of lattice structure, while a multiscale model is proposed to compute the yield strength. In particular, the multi-objective optimization including both the residual stress and support volume is discussed and investigated in this work. Experimental validation is conducted on a realistic component with some geometric complexity. By comparing the component and support structure without build orientation optimization, it is found that the proposed framework can significantly reduce the influence of the residual stress on the printed part, ensure the manufacturability of the design, and decrease the material consumption for the sacrificial support structure simultaneously.

Keywords: metal additive manufacturing, lattice structure, voxel-based mesh generation, particle swarm optimization, inherent strain method.

1. Introduction

The technology of interest in this work is powder bed metal additive manufacturing (AM), which has been widely accepted by industry to produce highly valuable component, such as customized implant, conformal cooling for mold manufacturing, fuel nozzle, etc. It is a manufacturing process that a laser or electron beam is used to selectively melt a metallic powder layer according to the contour of sliced computer-aided design (CAD) model, refer to Fig. 1. Once a layer of powder is melted and solidified, the build tray is moved downward, and a fresh layer of powder is uniformly deposited upon the previous layer for next build. The cycle of deposition, melting and solidification continues until the bulk component is completely manufactured. Since the laser/electron beam only melts the powders in selected locations based on the CAD model, it is possible to apply metal AM process to build components with complex geometry and realize functional performance [1].

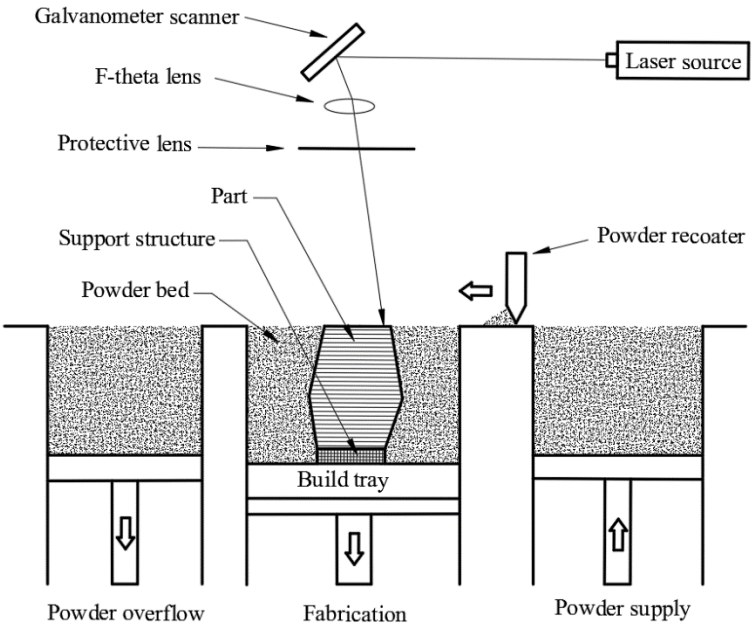

Fig. 1. Schematic view of powder bed metal AM process.

However, in practice, there are several issues preventing metal AM from broad adoption: Residual stress, and residual distortion introduced in powder melting and solidification processes [2-4]. Residual stress leads to undesirable cracks, delamination, and warpage during AM, which can stop the powder spreading process and result in failures of the builds. This not only lengths product manufacturing, leads to a waste of material, energy and time, but also requires extra efforts for designers to change the design. Figure 2(a) illustrates such issue, in which the cracked and deformed component stops the powder deposition, leading to a failure build. Another challenge is the large deformation generated by residual stresses after the component is removed from substrate. The deformation results in limited load resistance, dimensional inaccuracy, and reduction of fatigue performance of the component to more than 10 times compared with the conventional bulk material [5, 6]. As illustrated in Fig. 2 (b), an implant was successfully printed out in Ti6Al4V using laser powder bed AM, but once it was cut from the build tray, the inherent residual stresses lead to undesirable deformation.

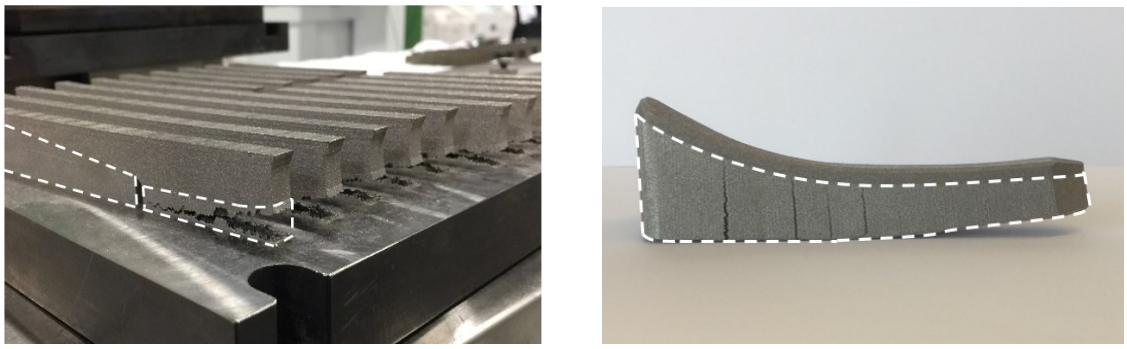

(a) (b)

Fig. 2. Residual stress and large deformation of metal AM: (a) failed build due to residual stress during the manufacturing; (b) implant is deformed after removal from the building chamber.

On the other hand, support structures (e.g. the structures highlighted by white dash line in Fig. 2) are required in metal AM to support overhangs of the component to ensure manufacturability. These support structures are fabricated simultaneously with the component to anchor the parts and dissipate heat to the build tray in order to prevent distortion/delamination caused by residual stresses. There is a number of published works in the past in the areas of support structure design for AM techniques. Allen et al. [7] proposed the best directional formation for an object to obtain minimal support structure. Frank et al. [8] developed an expert system tool to interact with users to select the best build orientation for better performance of the built component. Alexander et al. [9] developed a method to optimize part orientation to minimize build cost. Xu et al. [10] discussed the section of build orientation for four types of AM processes and proposed an orientation optimization with multiple criteria, such as building inaccuracy, manufacturing time and building cost. Lan et al. [11] developed an algorithm for stereolithography apparatus to find a desirable fabrication orientation for a given design based on considerations of surface quality, build time, and complexity of support structures. Masood et al. [12] presented a generic mathematical algorithm to find the best orientation to achieve minimum volumetric error. For fused deposition process, Thrimurthulu et al. [13] applied genetic algorithm to determine an optimum part deposition orientation to enhance part surface finish and reduce build time. Recently, Mumtaz et al. [14] developed a method for metal powder bed AM processes to eliminate the need for supports. Strano et al.[15] presented an approach to optimize part-built orientation and support cellular structure. Hussein et al.[16] experimentally investigated influences of low-volume fraction lattice structures on the design of support structure for powder-bed direct metal laser sintering (DMLS) machine. Galigonano et al. [17] applied Taguchi method to optimize support structure and conducted experiment to investigate the manufacturability of overhanging structures for SLM process. Most recently, Vaidya et al. [18] developed an approach for minimizing support structures with space cellular infill combined with Dijkstra's shortest path method to generate optimized support structure. Paul et al. [19] proposed a voxel-based framework to generate support structure and developed a multi-objective method to minimize support volume, the cylindricity and flatness errors simultaneously. Following the work of Paul [19], Das et al. [20, 21] proposed a method to minimize part errors in AM through the selection of build orientation for optimal support structures.

However, most of these previous researches focused on geometric perspectives, and few works have been proposed to take the residual stress into consideration for metal AM to ensure manufacturability. For simple geometry, the stress problem can be addressed by manually changing the build orientation through trail-and-error. For component with complex geometry, this empirical approach may not work, and more

effective methodology needs to be developed to minimize residual stress. Nevertheless, there are several barriers preventing development of such optimization method. First, due to the complexity of laser manufacturing process, it is time-consuming to obtain residual stress and distortion distribution through detailed process simulation. In general, it takes tens of hours or days to complete process simulation of a simple component in general. This makes it impractical to find optimal orientation considering hundreds of iterations required by the optimization methods. Second, mesh generation for complex geometry and its support structure is computationally expensive and often error-prone when pure Cartesian grids are desired, or when the bulk component is rotated in the printing space to seek optimal orientation and the layerwise mesh along the building direction is required. Third, problems arise when the mesh generation and finite element analysis (FEA) is considered for support structure. The typically used support structure consists of straight rectangular solid walls or cellular structure [7, 15, 16], which is self-support, lightweight and loose enough to be easily removed. However, from the simulation point of view, it is difficult to generate efficient mesh for these tiny structures, and thus leads to error estimation for residual stress in support structure where most cracks and delamination are observed. Due to these barriers, an efficient approach to ensure manufacturability of AM components through optimization of build orientation is difficult to achieve together with other objectives, such as surface finish [22], dimensional accuracy [7, 19], volume of support structure, [18-20] etc.

The aim of this work is to develop a robust computational framework to address the aforementioned problems by systematically optimizing the orientation of a component to reduce the maximum residual stress, and at the same time minimize volume of support structure to reduce manufacturing cost. There are two major contributions in this work. First, a voxel-based approach is developed to generate Cartesian mesh for both manufactured part and its support structures required for any part build orientations. Differentiating from previous works [19, 20], in this work, overhangs requiring support structure from stereolithography (STL) file are divided into three categories: Facets, edges, and points. Based on this new categorization, a geometry with extraordinary feature (i.e. pine feature) at any given orientation can be properly supported, with neither extra support [19] nor less support in [20]. Furthermore, a base plate whose dimension is equal to the envelope box of the bulk component is generated at the bottom of support structure for simulation. Second, a fictitious domain method [23-26] based-framework that integrates fast process simulation [27-30] with aforementioned Cartesian mesh generation, support structure detection and asymptotic homogenization [1, 31] is proposed to rapidly compute residual stresses within the built component and its support structures. This integration avoids the error-prone body-fit mesh generation, simplifies the complex thermomechanical process by a pure static mechanical analysis, and thus mitigates the expensive computation cost for simulation of the complex physics in metal AM for part-scale problem. In this work, three different lattice structures are studied for support structure design. In short, the obstacles mentioned in previous paragraphs are overcome, and making it possible to using optimization method to minimize maximum residual stress and volume of support through adjustment of part orientation.

The remaining content is organized as follows. In section 2, the voxel-based mesh generation and support volume calculation for any part orientation is introduced and compared with the previous works. Section 3 introduces the computational framework to perform analysis of AM component including the homogenization and multiscale model for lattice structure, and implementation of inherent strain method and finite cell method for fast process modeling. Section 4 describes the multi-objective optimization strategy to minimize maximum residual stress along with minimization of volume of support structure. In section 5, several numerical examples are studied and investigated based on the proposed optimization strategy, and the optimal designs are printed out for comparison purpose.

2. Voxel-based Support and Mesh Generation

One key step of minimization for support volume and simulation-based orientation optimization is the mesh generation. Especially when the bulk component is randomly rotated in the manufacturing space, the method that can rapidly generate mesh for both the component and its support structure along build direction is necessary. In general, conformal mesh is employed in finite element analysis (FEA) to provide accurate description. This is easy to achieve for component with simple geometry, while for structures of highly complex geometry (i.e. aerospace component for metal AM shown in Fig. 3), severe problems are encountered for conformal mesh generation [32]. It is because the translation from computer-aided design (CAD) model to finite element (FE) discretization is extremely computational expensive, and the generation of the conformal mesh is hardly automated and error-prone, which normally requires extra effort for trial-and-error by the users [24]. On the other hand, the generation of support structure for complex geometry based on CAD model is also time-consuming, due to the construction of support structure using thin wall features [21, 33] or lattice structures [16, 18, 34]. The mesh generation for these support structure can also lead to high computational cost, making it impractical to minimize residual stress and at the same time to minimize support volume for build orientation optimization. To circumvent these problems, a voxel-based methodology is employed and improved to automatically generate layerwise Cartesian mesh and support structure along the build direction, see the results in Fig. 3(c). Note that uniform voxel-based mesh is generated in this work, which may lead to large number of elements for FEA. To ensure the efficiency of the analysis, the selection of element size is based on the convergence study of h-version finite cell method (FCM) in [26].

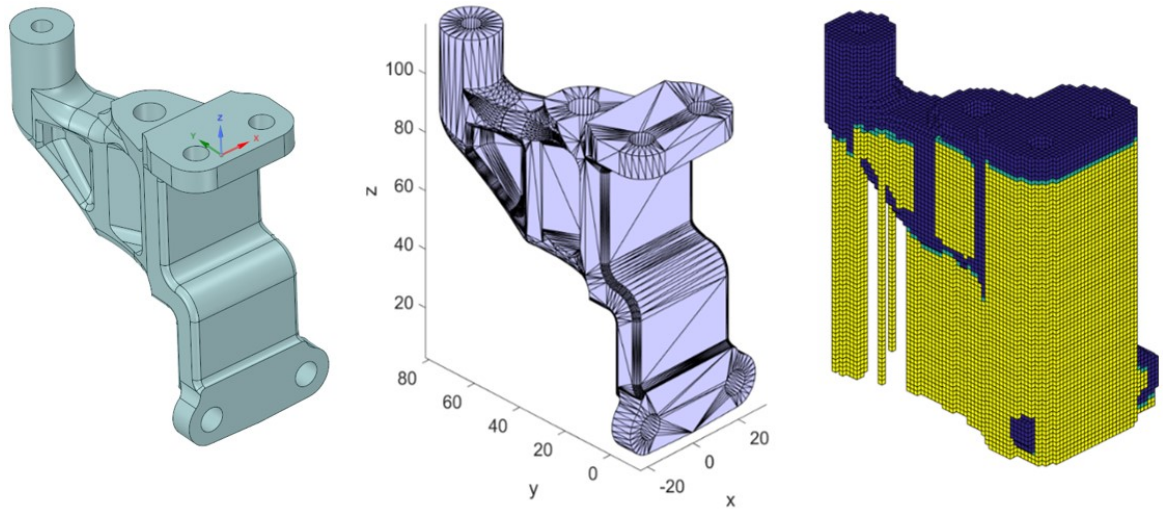

(a) (b) (c)

Fig. 3. Component for aerospace: (a) CAD model; (b) STL file; (c) voxel-based mesh and support generation.

The voxel-based support generation was first proposed by Paul et al. [19] to minimize support volume and reduce form errors in the AM process. Das et al. [20] further extended this approach to minimize support structure volume and support contact area, and at the same time, maximize support structure removal to satisfy all the GD&T callouts. The voxel-based approach converts Stereolithography (STL) file into voxel discretization using ray tracing methods [35, 36], and add support voxel based on the overhang facets detection. Although the facet overhang detection in Ref. [20] can reduce the support volume compared with the method in [19], it may lead to underestimation of the volume in the overhang structures that need to be

supported. An overhang benchmark is designed to illustrate the performance of these two previous methods. As illustrated in Fig. 4, there are four different overhang structures in the benchmark.

- Case 1. A horizontal overhang facet connected with two facets that satisfy the overhang angle. Support structure only needs to add under the horizontal facets.
- Case 2. A concave feature consisted of two facets that satisfy the overhang angle (i.e. 45° along the build direction) requirement. No support structure is needed for this feature.
- Case 3. A convex feature consisted of two facets that satisfies the overhang requirement but needs support structure added along the overhang edge.
- Case 4. A convex feature consisted of four facets that satisfies the overhang requirement but needs support structure added to the protruding point overhang.

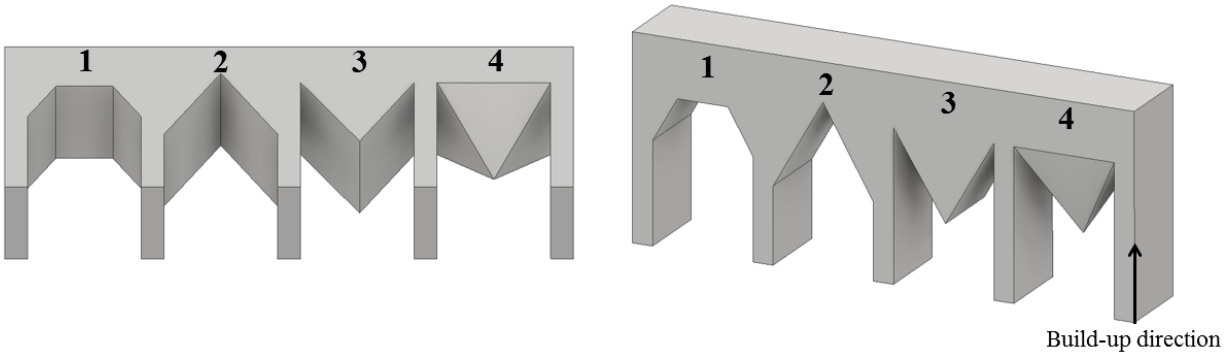

(a) (b)

Fig. 4. Benchmark of the overhang for voxel-based detection, (a) angled bottom view; (b) home view.

Using the method in [19], the overhang detections for the benchmark are highlighted in Fig. 5 (a) while the voxel-based support generation is illustrated in Fig. 5 (b). As can be seen, this method tends to support all the undercut discussed in Cases 1-4 and leads to an overestimation for the support structure calculation, making it difficult to remove support structure for metal AM.

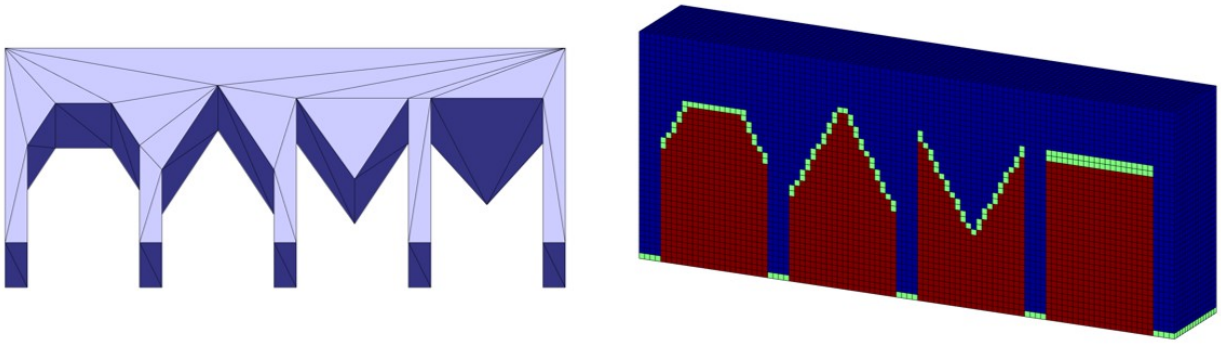

(a) (b)

Fig. 5. Overhang detection in [19] and its voxel-based support generation for benchmark: (a) overhang detection; (b) voxel-based support generation and mesh generation.

The overhang detection, voxel-based support generation according to the work of [20] are illustrated in Fig. 6. As shown in the figure, when only the facet overhangs are detected, support structure described in Cases 2, 3 and 4 is removed from the support voxel compared with the result in Fig. 5 (b). For edge overhang and

point overhang discussed in Cases 3 and 4, the support generated by this method is obviously an underestimation, because the floating structures in those two cases can lead to failure of an AM build.

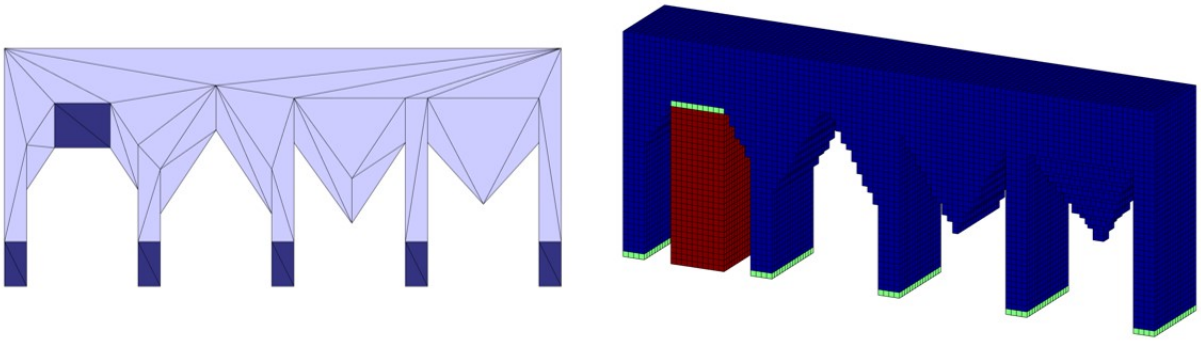

(a) (b)

Fig. 6. Overhang detection in [20] and its voxel-based support generation for benchmark. (a) overhang detection; (b) voxel-based support generation and mesh generation.

To address the issues of overhang detection in those previous voxel-based methods [19, 20], similar to the work of [34], the overhangs are divided into three categories: Facet overhang, edge overhang and point overhang, whose definition are given below:

- **Facet overhang** is a *downward triangular facet* in STL file which included angle $\theta(\boldsymbol{n}_i^f, \boldsymbol{n}_p)$ of its normal $\boldsymbol{n}_i^f$ to the printing direction $\boldsymbol{n}_p$ is not less than a threshold value, $\pi - \theta_f$, where θ_f denotes the smallest angle of a facet that can be printed without support structure. Figure 7(a) illustrates the definition of the included angle of facet about the printing direction $\boldsymbol{n}_p$, the corresponding 2D description is shown in Fig. 7(b). It can be seen when $\theta(\boldsymbol{n}_i^f, \boldsymbol{n}_p)$ is larger than the threshold value $\pi - \theta_f$ (i.e. $\frac{3}{4}\pi$), the included angle γ between the facet and the horizontal surface (i.e. the black dash line in Fig. 7(b)) is smaller than a critical value θ_f (i.e. $\theta_f = \frac{\pi}{4}$), which can lead to collapse of the manufacturing. Then, the facet i is labeled as a facet overhang and saved in set of O_f. Otherwise, the facet is grouped into self-supporting facets, which can be printed out without support structure.

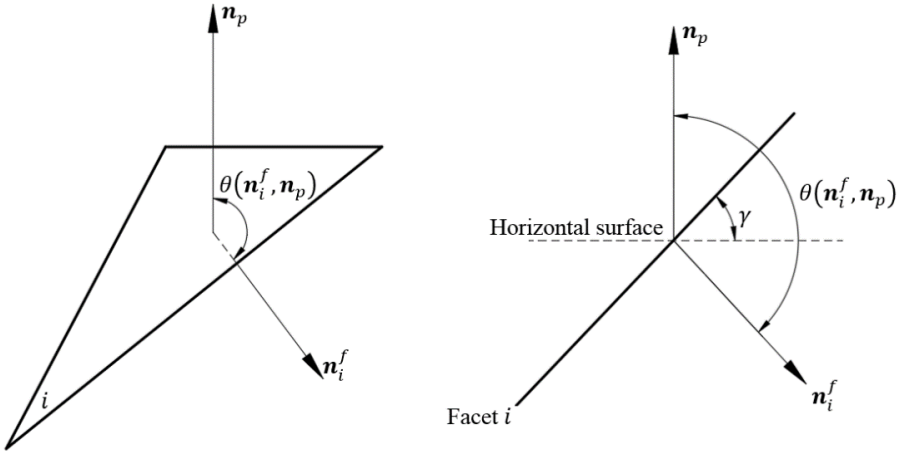

(a) (b)

Fig. 7. Definition of included angle of facet about the printing direction: (a) included angle of normal of i^{th} facet and printing direction, (b) 2D description of included angle for facet i.

- **Edge overhang** is a *downward convex* edges that do not belong to the facet overhang and at the same time the included angle between the normal of an edge $\boldsymbol{n}_j^e$ and the printing direction $\boldsymbol{n}_p$ is not less than a critical angle $\pi - \theta_e$, where θ_e is the threshold angle of edges that can be printed without support structures. Figure 8(a) illustrates the definition of the normal of edge j, which is the addition of normal $\boldsymbol{n}_{j1}^f$ and normal $\boldsymbol{n}_{j2}^f$, where $\boldsymbol{n}_{j1}^f$ and $\boldsymbol{n}_{j2}^f$ are the normal of two facets ($j1$ and $j2$) that are connected by edge j. As shown in Fig. 8(b), similar to the definition of facet overhang, when the included angle of edge normal $\boldsymbol{n}_j^e$ and printing direction $\boldsymbol{n}_p$ is larger than the threshold value, $\pi - \theta_e$, the edge is labeled as an edge that needs to be further analyzed for edge overhang; otherwise, the edge is safe for printing without support structures.

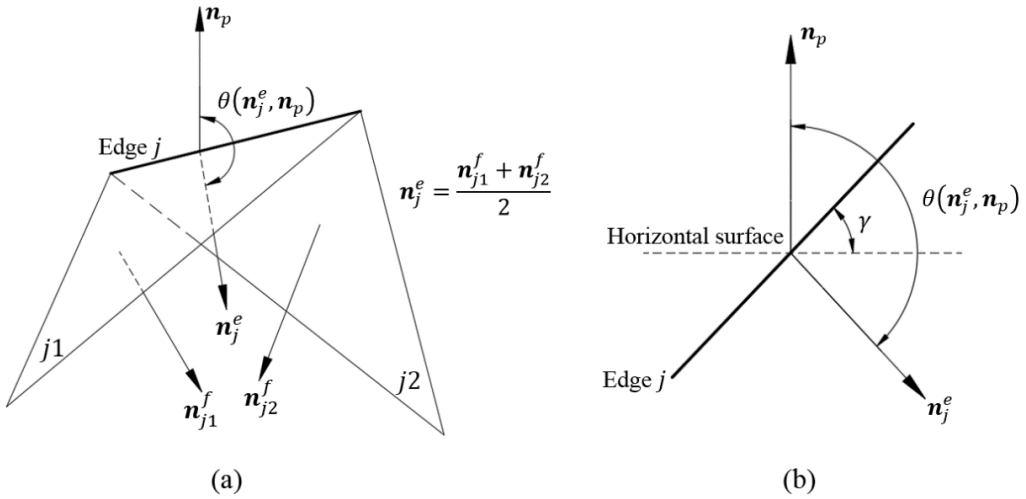

Fig. 8. Definition of the edge normal: (a) included angle of normal of j^{th} edge and printing direction; (b) 2D description of included angle for edge j.

In the work of [34], the definition of the edge normal is the average of the normal of its two incident facets. However, it is found that this definition may include some edges that satisfy the manufacturing requirement. As discussed in the four cases of benchmark, although the included angle of the edges in Case 2 and Case 3 are same, Case 2 does not need support structure while Case 3 requires support structure. To address this issue, an additional variable α_j for edge j is introduced and a constraint is added to distinguish edges in Case 2 and Case 3. The definition of introduced angle α_j is given in Fig. 9 and can be calculated using $\alpha_j = \theta\left(\boldsymbol{n}_{j1}^f, \boldsymbol{n}_{j2}^{j1}\right)$, where $\boldsymbol{n}_{j1}^f$ represents normal of facet $j1$ for edge j, $\boldsymbol{n}_{j2}^{j1}$ is a vector which tail is the point of facet $j1$ that is not on edge j and the head is the remaining point of facet $j2$, refer to Fig. 9(a). It can be seen when $\alpha_j \geq \frac{\pi}{2}$, the edge is a convex structure, while when $\alpha_j < \frac{\pi}{2}$, the edge is a concave structure. Thus, the additional constraint of $\alpha_j \geq \frac{\pi}{2}$ is added to ensure only the downward convex edge is identified in the edge overhang detection.

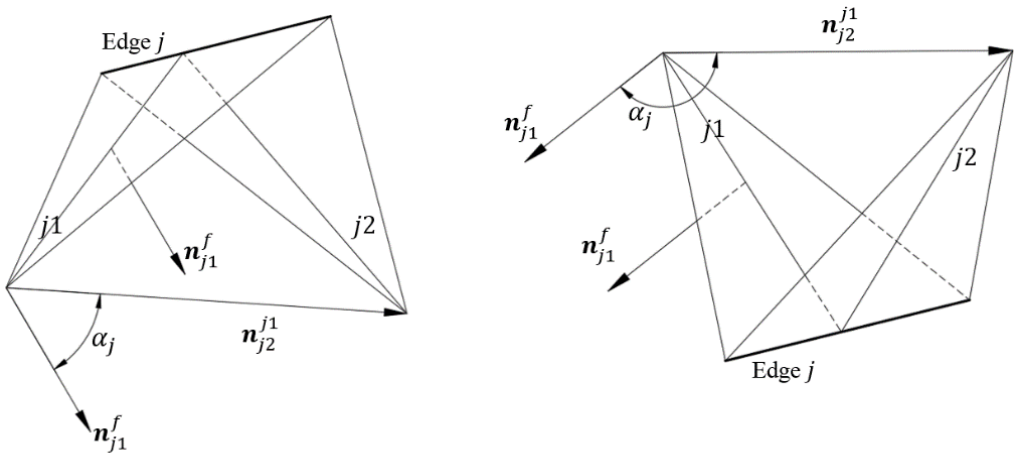

Fig. 9. Edge with the same normal but different support requirement: (a) downward concave edge without requirement of support structure (b) downward convex edge needs to be supported.

- **Point overhang** is a point on the downward facet that is lower than its neighbor points and at the same time belongs neither to the facet overhang group nor to the edge overhang.

Once the overhang facets, edges and points are detected based on the three schemes, the ray tracing method [35, 36] is employed to generation voxels for the bulk component and its support structures. By using the new detection methodology, the overhang detection and voxel-based support and mesh generation are given in Fig. 10(a) and (b), respectively. It can be seen both the downward convex edge overhang and point overhang are identified and the corresponding support voxel is added in the voxel design. Comparing with the previous method, the new methodology can provide more accurate support volume calculation and voxel mesh generation for the analysis.

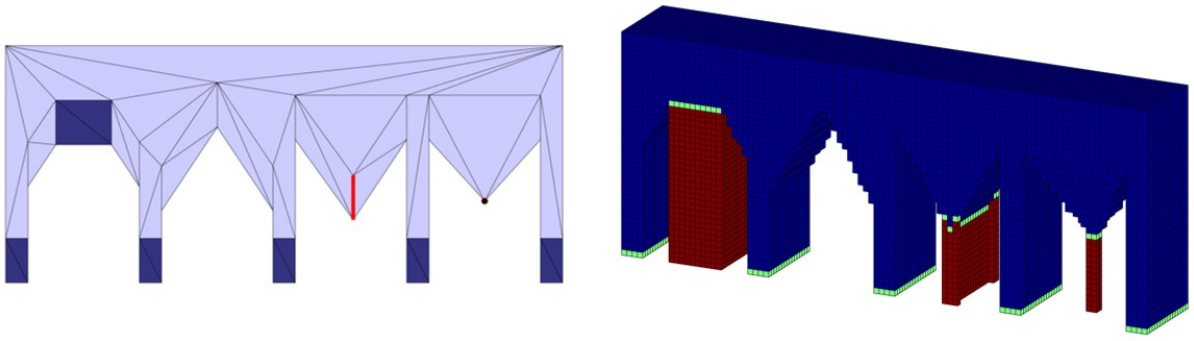

Fig. 10. New overhang detection and voxel-based support generation for benchmark: (a) overhang detection; (b) voxel-based support and mesh generation.

It is noted that the software code for overhang detection and voxel mesh generation for both solid part and support structures is developed and implemented in MATLAB 2016a. There are three main functions for the implementation. First, a function is developed to read STL file and detect overhang faces, edges and points based on the norms of triangle facets of a given STL file. Second, a function of ray tracing method is developed to covert the STL file to voxel representation, in which the voxels corresponding to the detected overhang features are labeled (e.g. the yellow voxels in Fig. 10 (b)) for support generation. Third,

based on the labeled voxels, a function is developed to generate support voxels and combine with part voxels obtained from previous function to form Cartesian mesh for FCM analysis.

3. Voxel-based Fast Process Modeling for Calculation of Maximum Stress

3.1 Mechanical Properties of Lattice structure: Elasticity and Plasticity

In this work, lattice structure is used as the support material to dissipate heat and provide strength to anchor the bulk component to the substrate. Comparing with the block shell support structure widely used for metal AM, refer to Fig. 11(a), the prominent characterization of lattice structure is its open-cell and self-support nature. This makes it an ideal material for support structure, since it can be printed out without support structure and also allows the trapped powder to be easily removed. Although lattice structure is an efficient material for support structure, it is computationally expensive to explicitly perform full-scale simulation to model the microstructural feature of lattice structure for metal AM. The major challenge is the mesh generation and considerably computational cost for detailed simulation on the microstructure of lattice materials.

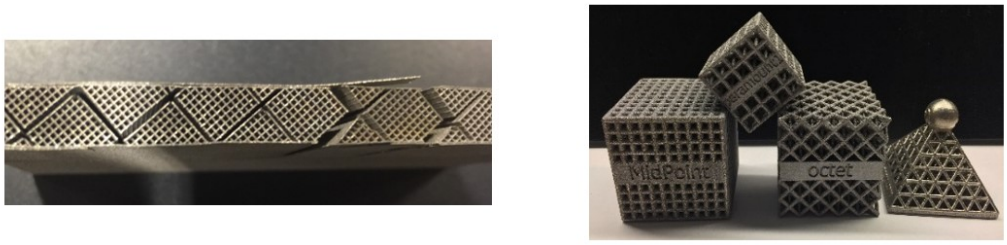

(a) (b)

Fig. 11. Structure for support structure: (a) block shell support structure; (b) lattice structure.

To avoid time-consuming computation for lattice structure, asymptotic homogenization (AH) [37, 38] method is employed to compute the effective elastic properties of lattice structure, while a multiscale model [31] is proposed to capture the anisotropy. By performing analysis on representative volume element (RVE) of lattice structure, a homogenized model is developed to treat lattice material as continuum material with equivalent properties. This simplifies the analysis concerning microstructural feature of lattice structure to analysis based on the homogenized model. Thus, full-scale simulation on lattice structure is circumvented by utilizing equivalent properties obtained from homogenized model to the elements in the support design domain. This makes it possible to conduct optimization to iteratively find the optimal orientation to minimize maximum residual stress. Appendix A details the AH method used to compute both effective elastic properties and yield strength of lattice material based on the analysis on RVE model. Detailed information on the AH method can be found in Refs. [1, 31, 38].

In this work, to study the influence of microstructure of lattice materials on residual stress of the AM component, three different types of lattice structure are studied. As shown in Fig. 12, the three lattice structures are cubic, cross, and diagonal. The major difference of these three lattice structures is that the “cross” lattice added crossing ligaments to the faces of the “cubic” lattice, while the “diagonal” lattice adds crossing ligaments to the diagonals of the “cubic” lattice. We would like to investigate the influence of the distribution of ligaments on the stress distribution. Figure 12 (d) illustrates support structure design for the overhang benchmark mentioned in Section 2 using cubic lattice structure.

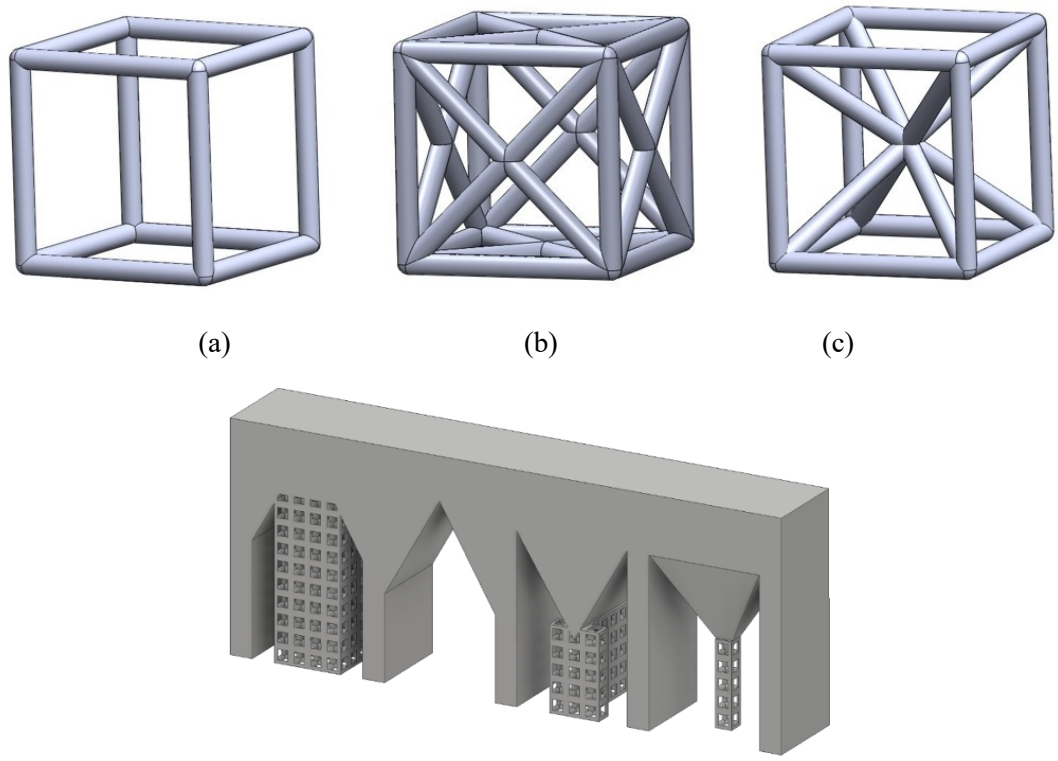

(a) (b) (c)

(d)

Fig. 12. Lattice structure used for support design: (a) cubic, (b) cross, (c) diagonal, and (d) support structure design for overhang benchmark.

3.2 Inherent Strain Method for Fast Prediction of Residual Stress

Powder bed metal AM is a process to selectively melt metal powder in a layer-by-layer fashion according to the contour of the sliced CAD model. Once one layer of powder is melted and solidified, a fresh layer of powder is spread by a roller while the melting and solidification process is repeated until the entire part is successfully manufactured. Although metal AM technique has the ability to fabricate parts with complex geometry, residual stress induced failure is a severe issue for this advanced technology. As explained in [2, 39, 40], two mechanisms introduce residual stresses into the build component at mesoscale, refer to Fig. 13. At first, when a single layer of powder is rapidly scanned by the laser beam, a transient heat is input on the upper surface and leads to a steep temperature gradient. The heated layer tends to be freely expanded. However, due to the restriction of the surrounding area, an elastic compressive strain is introduced on the top surface. When the yield strength of the material is reached, plastic compression will occur on the top layer, as shown in Fig. 13(a). Second, in the cooling process of the molten top layer, the heated layer tends to shrinkage due to thermal contraction. Owing to the inhibition of the underlying material, the shrinkage is prevented, and a tensile stress is introduced on the top of the added layer, refer to Fig. 13(b). In the entire manufacturing process, each layer may experience several heating and cooling cycles at inconsistent level, which leads to the accumulation of the residual stresses, and thus the undesirable large deformation, cracks, delamination, etc.

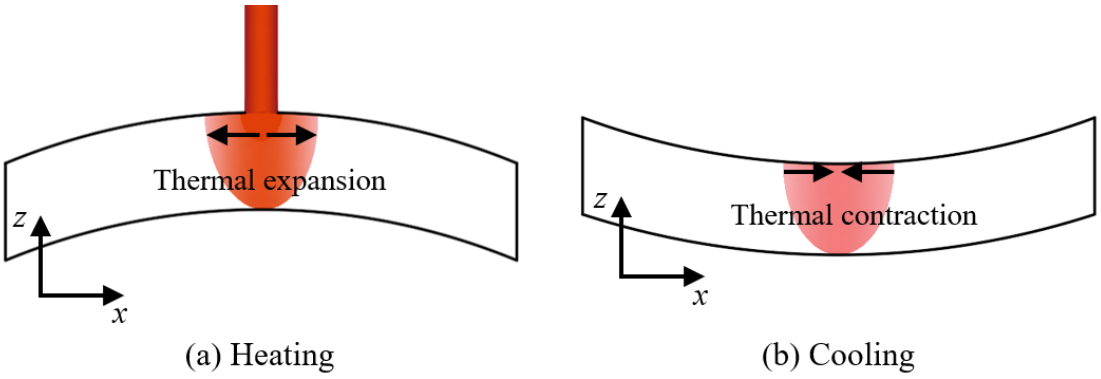

Fig. 13. Two mechanisms of residual stresses generation at mesoscale

Build orientation plays an important role in residual stresses accumulation, since it determines the support structure generation and thus the distribution of stress and strain introduced by the manufacturing process. Consider the dogbone shown in Fig. 14(a) as an example. The dogbone is built in three different directions (i.e. 0°, 45° and 90° by y-axis, refer to Fig. 14 (b-d)) with support structures added to support overhanging structures, which are detected by the method proposed in Section 2. It can be observed that the support structures vary a lot among the three build orientations. This illustrates that as the build orientation is changed, the manufactured volume, especially the support structure volume, is changed. To examine the influences of the build orientation, fast process simulation by using the inherent strain method [27-30] is performed to calculate the residual stress distributions for the three build orientations. Figure 14 (e-g) show the three residual stress distributions. As can be seen, the maximum normalized residual stress by Hill's stress measure (refer to Appendix A) of the horizontal orientation in Fig. 14(e) is 2.30, the maximum value of orientation 45° in Fig. 14 (f) is 1.62, and the maximum value of orientation 90° in Fig. 14 (g) is 1.14, in which the vertical orientation in Fig. 14 (g) exhibits the smallest maximum residual stress comparing with another two build orientations. This demonstrates that build orientation has significant influence on the residual stress distribution. Hence, it is possible to address the residual stress induced failure through optimization for the build orientation.

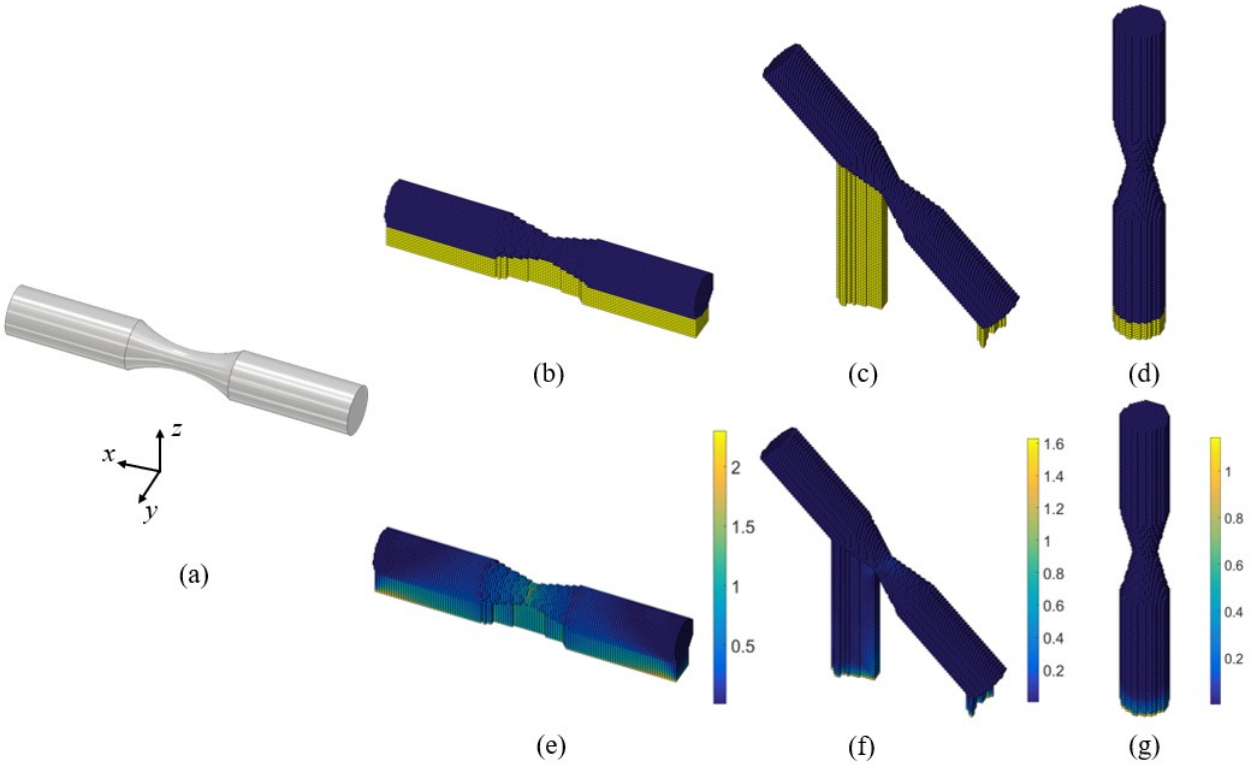

Fig. 14. Influence of build orientation on a generic dogbone. (a) CAD model of a dogbone (b) mesh of the dogbone is oriented 0° by y-axis (c) mesh of the dogbone is oriented 45° by y-axis (d) mesh of the dogbone is oriented 90° by y-axis; (e) normalized residual stress distribution of 0° orientation (f) normalized residual stress distribution of 45° orientation (g) normalized residual stress distribution of 90° orientation.

However, it is challenging to perform iterative optimization for residual stress minimization due to the expensive computational cost for both mesh generation and simulation for full-scale thermomechanical process. For the former challenge, voxel-based Cartesian mesh generation proposed in Section 2 is used to circumvent the mesh generation issue. While for the second challenge, the most accurate way for residual stress estimation is to perform detailed simulation where the powder melting and solidification process is modeled in detail based on the printing strategy. It has been proved that such high-fidelity analysis can provide accurate prediction for temperature history and deformation field [41-45]. Nevertheless, this type of simulation takes tens of hours for even a small-scale build and makes it impractical for part-scale problem. To make the proposed optimization method practical, the inherent strain method is employed in this work to efficiently simulate residual stress inherent in the DMLS process. There have been a number of published works regarding the development of this method for AM. Keller et al [46] developed a multi-scale approach to extract inherent strain tensor components and implemented the inherent strain method by pure mechanical simulation. Good agreement was observed between computed distortion and experimental measure in their work. Li et al [40] developed a multi-scale finite element model for fast prediction of distortion of parts manufactured by selective laser melting (SLM) process; however, no details were given on how to extract the inherent strain tensor in this work. Recently, Bugatti et al [29] developed a finite element AM simulation based on the inherent strain method and discussed the limitations and strengths of inherent strain method for prediction of residual deformation in metal AM through experiments. As illustrated in this work, the difference for the prediction of residual distortion between the calibrated inherent strain method and experimental measure is less than 100 μm. Liang et al [28, 47] proposed a

modified inherent strain method for laser engineered net shaping (LENS) and conducted experiments to validate the predicted residual distortion. Based on Liang et al [28, 47], a maximum of 10% error for the predicted residual distortion is observed. Setien et al [48] presented an empirical methodology to determine inherent strains and validated it using the twin-cantilever beam made in Ti6Al4V alloy. Bilal et al [30] experimentally showed that residual stresses predicted by inherent strain method agree well with the value measured by contour method. Marvin et al [49] applied X-ray diffraction to measure the residual stress for a small test samples and compared with the prediction from inherent strain method. It is found that the inherent strain method provides reliable prediction of residual stresses.

Although the inherent strain method has been employed to simulate residual stress and distortion of AM components, there are two major limitations of the existing methodology. First, the prominent feature of the inherent strain method is its replacement of the complex thermomechanical process by a pure mechanical analysis. This simplification results in lack of detailed information regarding thermomechanical history of the printing process. Second, the inherent strain method is based on the assumption of continuum description for powders in the simulation. This neglects the powder distribution and makes it impractical to simulate morphology of melting pool, evolution of microstructure, as well as the local defects (e.g. less-fusion, porosity, spatter, denudation, keyholing) for an AM part. However, the goal of this work is to develop an optimization method for build orientation to address the residual stress induced build failure at part-scale level. Hence, the limitations of inherent strain method at microscale are neglected, while the unique capability of inherent strain method for efficiently simulating residual stress for larger model is utilized to perform build orientation optimization. For detailed theory and validation for the inherent strain method, readers are referred to Refs. [28, 30, 49]. With regard to implementation of the proposed method, the fictitious domain method [50-52] (i.e. finite cell method (FCM)) is applied to perform inherent strain method and compute residual stresses. The FCM method belongs to the fictitious domain method/immersed boundary method (IBM) and proposed by Parvizian et al [26] to avoid error-prone conformal mesh generation. It has been successfully applied to solve various problems, such as non-linear analysis [24], transport problem in porous media [53], biomechanical analysis [23, 54], etc. The detailed implementation of FCM for inherent strain method is given in Appendix B.

4. Optimization Model for Minimizing Support Structure Volume and Residual Stress

In the Sections 2 and 3, the methodology for calculating support structure volume and residual stress have been explained. Open-cell lattice structure is used as the support structure to anchor the solid component to build tray. When the volume fraction of the support structure is set to a constant value (e.g. $V = 0.3$) to ensure manufacturability, both the volume of support structure and stress distribution are assumed to be solely determined by the build orientation. This makes it possible to minimize the volume of support structure while reducing maximum residual stress simultaneously. However, these two objectives may conflict with each other. A build orientation optimized for support volume may lead to a reduction of support volume but result in an increase of maximum residual stress. To address the conflict between these two objectives, a multi-objective optimization model is proposed here to optimize the build orientation in order to minimize the maximum residual stress along with the total volume of the support structure by a weighting function. Hence the maximum stress and the volume of support structure are combined using a linear function to form a single weighted aggregate optimization. The definition is given as follows:

$$F(\theta, \phi) = w\lambda V_s(\theta, \phi) + (1 - w)\bar{\sigma}^H_{max}(\theta, \phi) \tag{1}$$

$$s.t. \quad \mathbf{KU} = \mathbf{F}^{in}$$

$$-\pi \leq \theta < \pi \tag{2}$$
$$-\pi \leq \phi < \pi$$

where θ and ϕ are the angles by which the part is rotated about x and y axis, respectively, and $F(\theta, \phi)$ represents the combined objective function; V_s is the volume of support structure calculated from support voxel; $\bar{\sigma}_{max}^{H}$ denotes the normalized maximum residual stress in the domain including both the support structure and bulk component. w is the weighting value used to provide the flexibility to vary the contribution of the different objectives to the combined objective function. λ represents the scaling factor used to ensure that the support volume is within the same order of magnitude as the maximum stress. The two inequalities in Eq. (2) impose the constraints of the rotation angle about the *x* and *y* axes. Note that z axis is assumed to be the printing direction.

Since the explicit mathematical model between the objective function in Eq. (1) and design variables are difficult to obtain, the heuristic optimization method named particle swarm optimization (PSO) [55] is employed to find the optimal solution. For multi-objective optimization problem, due to the conflict among competitive objectives, there exists more than one optimal solutions, which are referred as Pareto Optimal solutions [56]. The solutions within the Pareto Optimal solutions are considered equally optimal. Particularly in this work, the solutions with minimum height are selected as the optimal design since the manufacturing time is determined by the height of the part. The lower the part, the less the time it takes to print.

5. Numerical Examples and Experimental Validation

For validation purpose, a realistic industrial component is used to investigate the performance of the proposed orientation optimization framework. The aims of the investigation include studying the effects of 1) three overhang strategies on the minimum support volume calculation, 2) different types of lattice structures on the minimization of maximum residual stress, and 3) multiple objective optimization on the final design. To examine the performance of the optimal design for stress minimization, the designed component is printed out by the EOS M290 DMLS system in Ti6Al4V and compared with the non-optimal design and default design provided by the Magics software widely used for inserting supports into a build prior to printing.

The material properties of Ti6Al4V is used in the analysis include Young's modulus ($E = 110$ GPa), Poisson's ratio ($\nu = 0.3$), and yield strength ($\sigma_y^* = 1{,}060$ MPa). Without losing generality, the stresses illustrated below are normalized by the material's yield strength. When the local normalized stress is larger than 1, the material is undergoing plastic deformation; when the stress is smaller than 1, the stress state is elastic. The new overhang detection algorithm proposed in Section 2 is applied to compute the support volume. The inherent strain method, coupled with homogenized model of the lattice structure (introduced in Section 3), is employed to compute residual stress of the support domain and bulk component domain very efficiently. To ensure manufacturability of the support design, the volume fraction of the support structure is set to be $V = 0.3$, and the lowest point of the component to the build tray is 7 mm for the purpose of component post-removal. Particle swarm optimization (PSO) method is applied to solve the optimization problem in Eq. (1-2) [55]. The optimization is terminated when the change of the objective function within five successive iterations is smaller than 1×10^{-3} while the minimum iteration number constraint (i.e. 10 iterations at least) is satisfied. The FCM method for executing the inherent strain method and multi-objective PSO method are implemented using MATLAB 2016a. Generation of the lattice structure support is conducted by an in-house software code based on the application programming interface (API) of Autodesk Inventor Professional 2018. The computer with configuration of 7-core Intel(R) Xeon(R)

CPU E5-2687 v3 @ 3.10 GHz is used for the mesh generation, FCM analysis, and optimization. Without specific notation, the computational cost discussed in the following section is calculated in this computer.

5.1 Minimization of the Support Volume Based on the Proposed Overhang Detection

In this case, a realistic industrial component is taken as the objective to compare with the three overhang detection methods described in Section 2. Figure 15 illustrates the CAD model and STL file of the bearing bracket used for the investigation. As shown in the figure, the bracket has two major features: One is the cylinder, which has an inner diameter of 18 mm and external diameter of 30 mm; the other is the base plate including two bolt holes used to fix the whole structure, whose dimension is $48 \times 36 \times 8\ \text{mm}^3$. The two features are connected by a rib structure with a constant thickness of 8 mm. Due to its complexity, it is difficult to empirically determine the optimal orientation of the component to minimize support volume and maximum residual stress simultaneously. This case mainly focuses on the minimization of support volume and w in Eq. (1) is equal to 1. Hence, the optimization problem becomes a single support volume optimization for finding the optimal build orientation. Considering the symmetry of the component along the $x-z$ plane, the ranges of the rotation of the part are $\theta \in [-\pi, \pi]$ and $\phi \in [0, \pi]$, respectively. In the optimization, 32 points are being uniformly distributed in the design domain as the initial particles for the PSO method. The three overhang detection schemes introduced in Section 2 are employed here for comparison purpose.

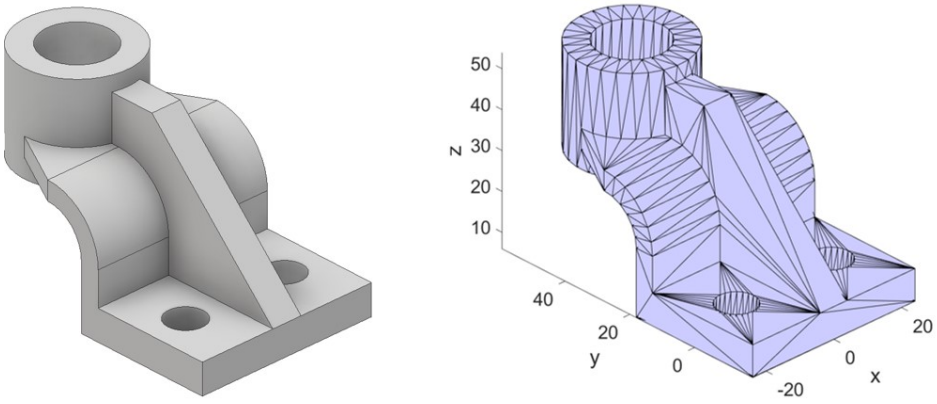

(a) (b)

Fig. 15. Bearing bracket for investigation of the optimization framework. (a) CAD model (b) STL file.

Figure 16 illustrates the initial state of the particles for the PSO method, the convergence history of the best position and the optimal support design with the build tray. The black dots given in the contour plot of Fig. 16(a) and the surface plot of Fig. 16(b) are the orientations of the particles. As shown in Fig. 16(a) and (b), there exists many local optima in the searching space according to the initial particles. By moving these particles using the PSO method, the objective function goes from $4.511 \times 10^4\ \text{mm}^3$ to a converged value of $4.132 \times 10^4\ \text{mm}^3$, or a decrease of 8.4%. The optimal orientation of minimum support volume is given in Fig. 16(d), in which the orientation is $(\theta, \varphi) = (\pi, \frac{\pi}{2})$.

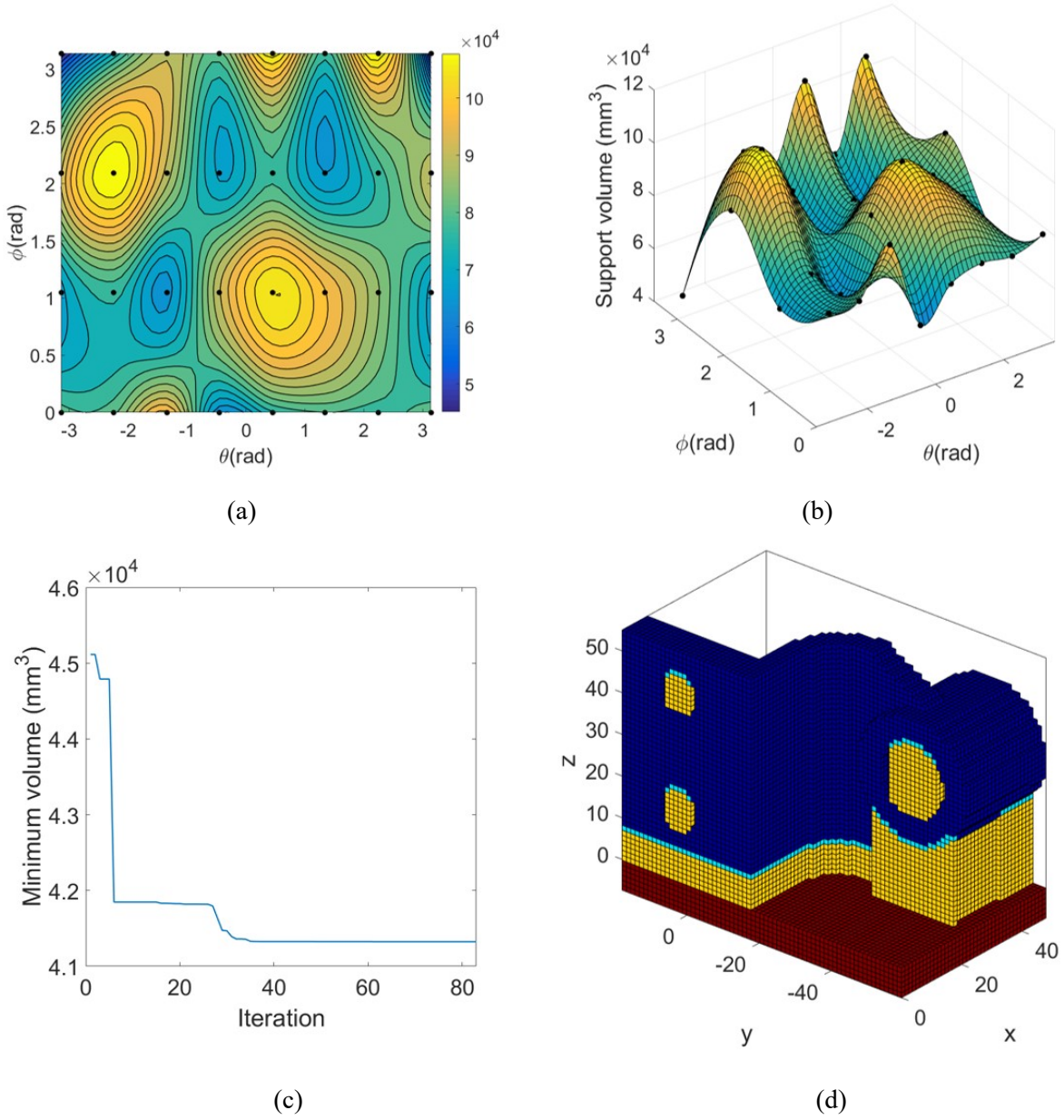

Fig. 16. Result of support volume minimization using the method in [19]. (a) Contour plot of the support volume at initial state (b) Surface plot of the support volume at initial state (c) Convergence history of best objective function at each iteration (d) Optimal support design.

The results based on the facet overhang detection proposed in [20] are shown in Fig. 17 including contour plot and surface plot of initial state of the support volume. For comparison purpose, the initial orientations of the particles are identical to the previous one. As can be seen, due to the change of the overhang detection, the initial distribution of the support volume in Fig. 17(a) and (b) is different from the previous one. After 40 iterations, the support volume is reduced to zero and the orientation coordinates are (θ, ϕ)=(0.7192, 2.7842). As shown in Fig. 17(d), since at the optimal orientation, no facet overhang is detected, and the bulk component is suspended on the build tray, which is not feasible. This shows that the single facet overhang detection strategy cannot guarantee successful support generation.

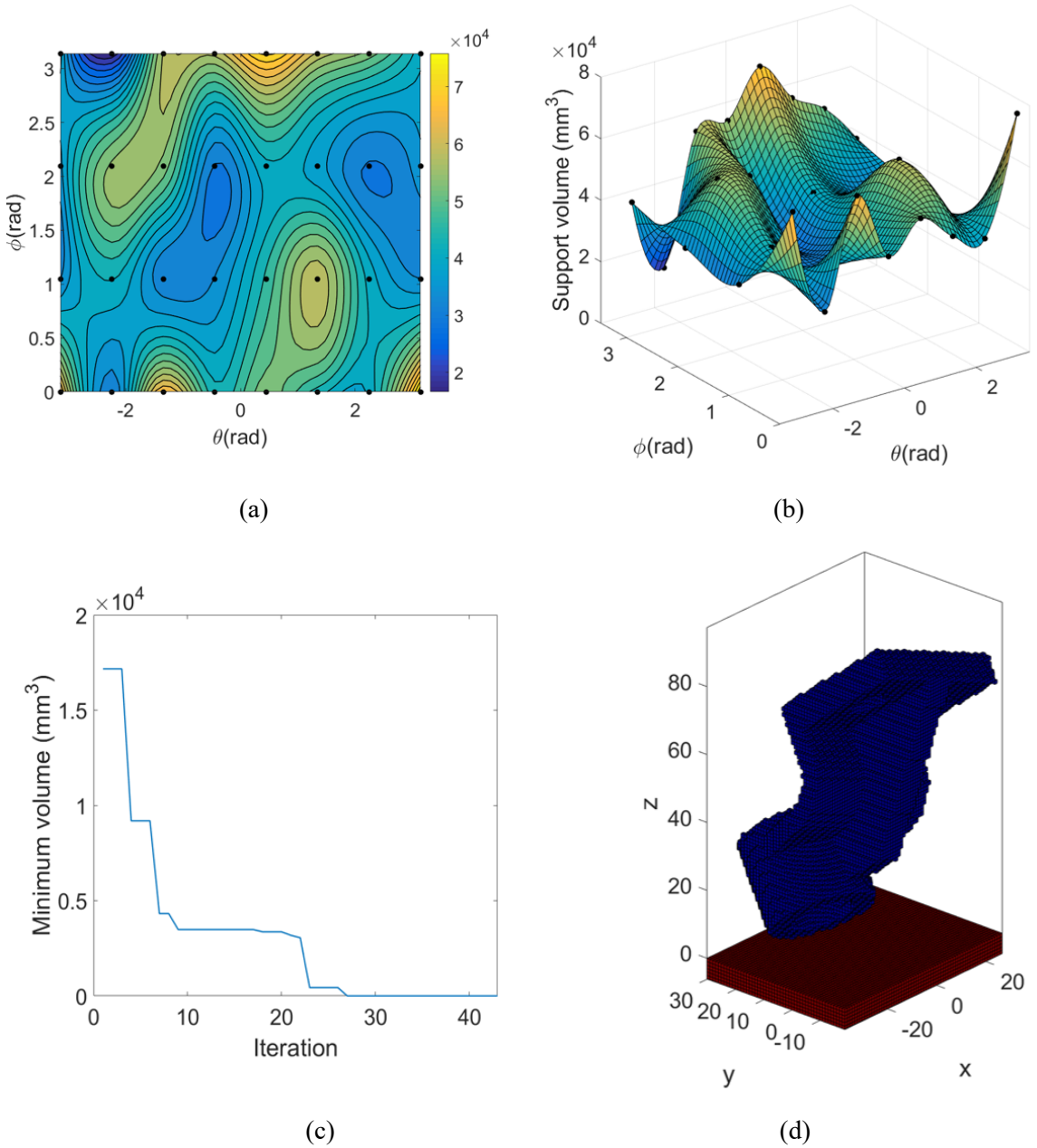

Fig. 17. Result of support volume minimization using the method in [20]. (a) Contour plot of the support volume at initial state (b) Surface plot of the support volume at initial state (c) Convergence history of best objective function at each iteration (d) Optimal support design.

The optimization result using the overhang detection proposed in this work is given in Fig. 18. Comparing with the other two methods, the initial contour plot and surface plot are similar to the results shown in Fig. 17 (a), but the optimal result is much different due to the detection of edge and point overhang. The minimum support volume of the particles converges from 2.104×10^4 mm^3 to 6.988×10^3 mm^3 , or a decrease of 66.8%, and the optimal orientation is $(\theta, \phi) = (-2.356,\ 3.130)$. The optimal orientation obtained by the proposed methodology is different from the previous methods.

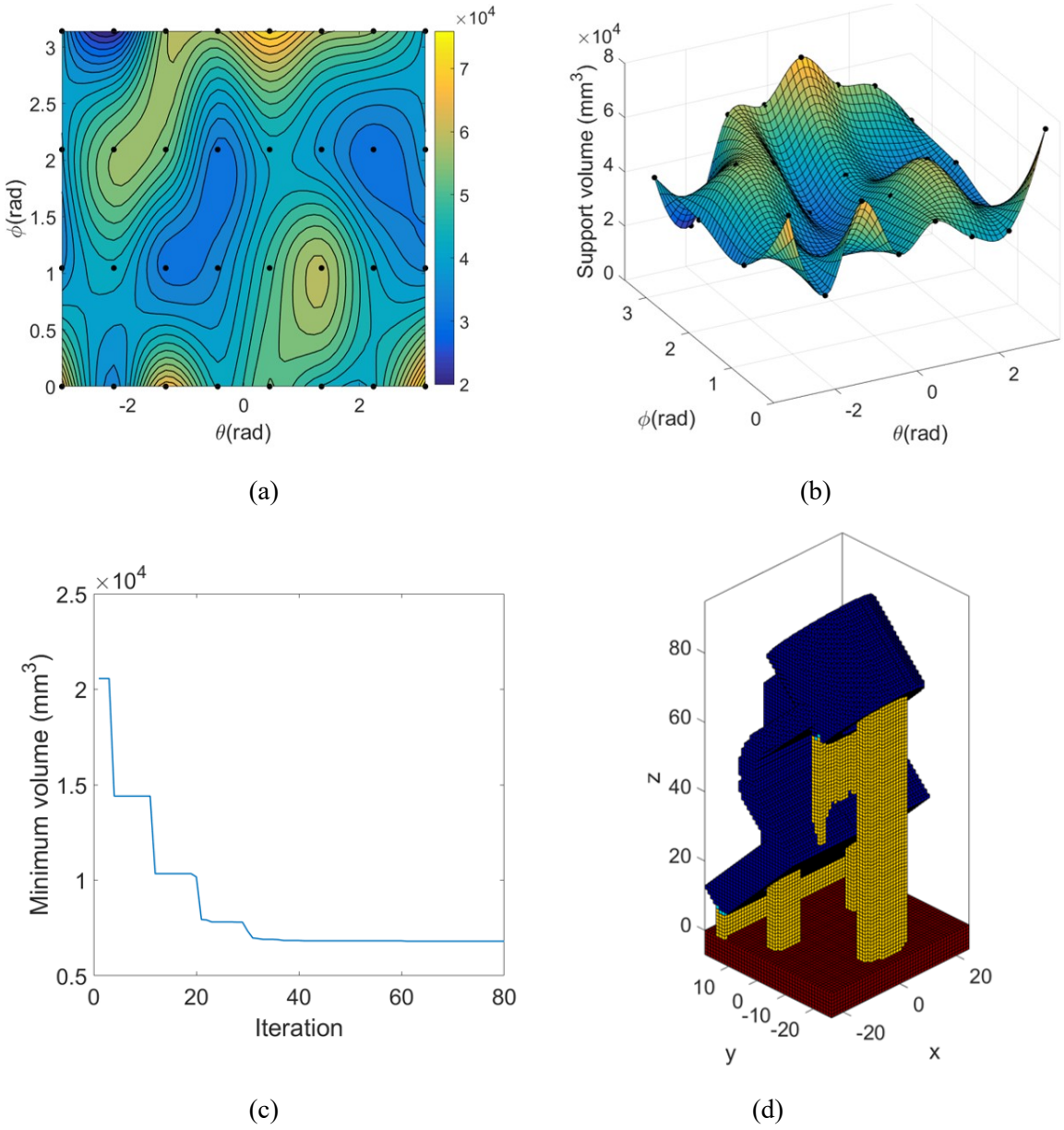

Fig. 18. Result of support volume minimization using the new method. (a) Contour plot of the support volume at initial state (b) Surface plot of the support volume at initial state (c) Convergence history of best objective function at each iteration (d) Optimal support design.

The mesh generation was performed on the computer with 7-core CPU. The computation cost of voxel mesh generation, overhang detection and volume calculation for the bearing bracket using the in-house MATLAB code was 0.5644 seconds per orientation, which equates to 24.08 mins in total for 80 iterations shown in Fig. 18. For comparison purpose, the bearing bracket was meshed by body fit mesh of the same element size (e.g. 1 mm) and the same number of computer cores using ANSYS v18.2. The computation cost was 6 s and so is 11 times longer than the proposed voxel mesh generation. This implies that the proposed voxel-based support structure detection and mesh generation is much faster than the body-fit mesh method and makes it desirable for support volume calculation and mesh generation for iterative optimization.

5.2 Study of the Design with Different Lattice Structure

In this sub-section, the single objective of minimizing maximum residual stress is performed based on different types of lattice structures given in Fig. 12. The bearing bracket used in the previous case is utilized to compare the influence of microstructure of lattice structure on the optimal orientation for minimization of maximum stress. Note that the volume fraction of lattice structure is set to be $V^* = 0.3$ to ensure manufacturability. In the optimization, there are 18 particles uniformly distributed in the design domain (i.e. 6 points for $\theta \in [-\pi, \pi]$, and 3 points for $\phi \in [0, \pi]$). The goal of the optimization is to minimize the maximum residual stress through the adjustment of build orientation on the build tray. For comparison purpose, the stress distributions of bearing bracket with the support structure consisting of the three lattice structures at default position are illustrated in Fig. 19(a-c). It can be seen that although the stress distributions are different, the larger stresses are mainly distributed at the bottom surface of support structure along the build tray, where most cracks are typically formed in the AM process. The maximum normalized residual stresses for three lattice structures are much higher than the yield strength of unity (i.e. 1.71, 1.85 and 2.02, respectively). This can lead to severe delamination and warpage during the printing process.

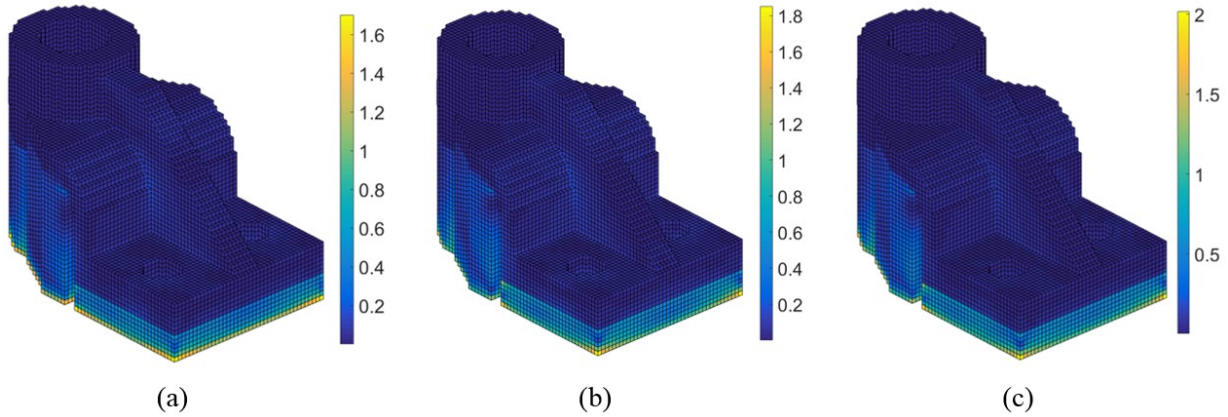

Fig. 19. Normalized stress distribution of bearing bracket with support structure consisting of different lattice structure. (a) Cubic lattice structure,$\bar{\sigma}^H_{max} = 1.71$, (b) Diagonal lattice structure, $\bar{\sigma}^H_{max} = 1.85$ (c) Cross lattice structure, $\bar{\sigma}^H_{max} = 2.02$.

To examine the efficiency of the inherent strain method, the three designs with lattice structure as their support, as well as the design with default support structure provided by the Magics software are printed out for deformation observation. Figure 20 illustrates the CAD models of the four designs. It is noted that the design of support structure from the Magics software is the default setting with a volume fraction of 0.4.

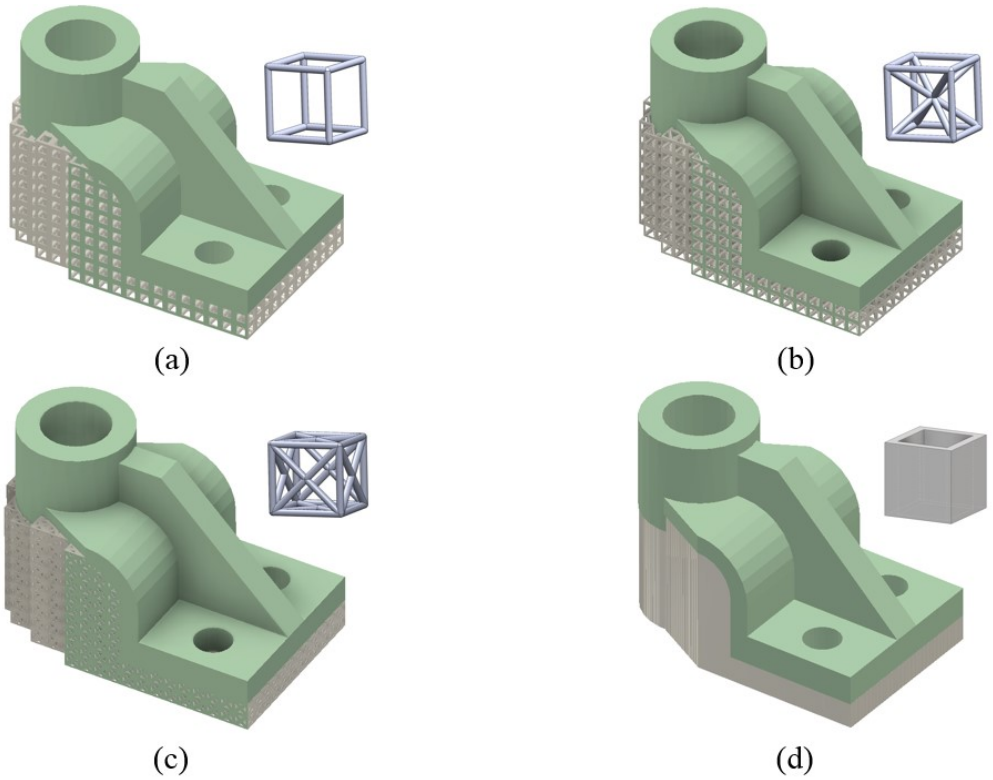

Fig. 20. CAD model of the bearing bracket with support structures for printing test: (a) design of cubic lattice support structure (b) design of diagonal lattice support structure (c) design of cross lattice support structure (d) design of shell wall support structure from Magic software.

For validation purpose, the four designs in Fig. 20 were printed out and the samples are illustrated in Fig. 21. As shown in the figure, although the bearing brackets were "successfully" manufactured using powder bed metal AM, cracks and large deformation are observed and highlighted by red box. Compared with the default support structure design from the Magics software, the designs with lattice structure support exhibit better performance for the deformation control. For instance, the support from the Magics software detaches from the build tray and has severe cracks and delamination for the manufactured part, see Fig. 21 (b), while the design with lattice structure support shows relatively small deformation. On the other hand, although lattice support structure can significantly reduce the deformation of the part, warpages are observed at the bottom surface of the bracket around the corners of the horizontal plate. It is consistent with the stress distribution in Fig. 19, where the maximum stress emerges near the corners of the bottom surface. This demonstrates that the proposed fast process modeling framework can provide good guidance to possible build failure for the laser powder bed AM process.

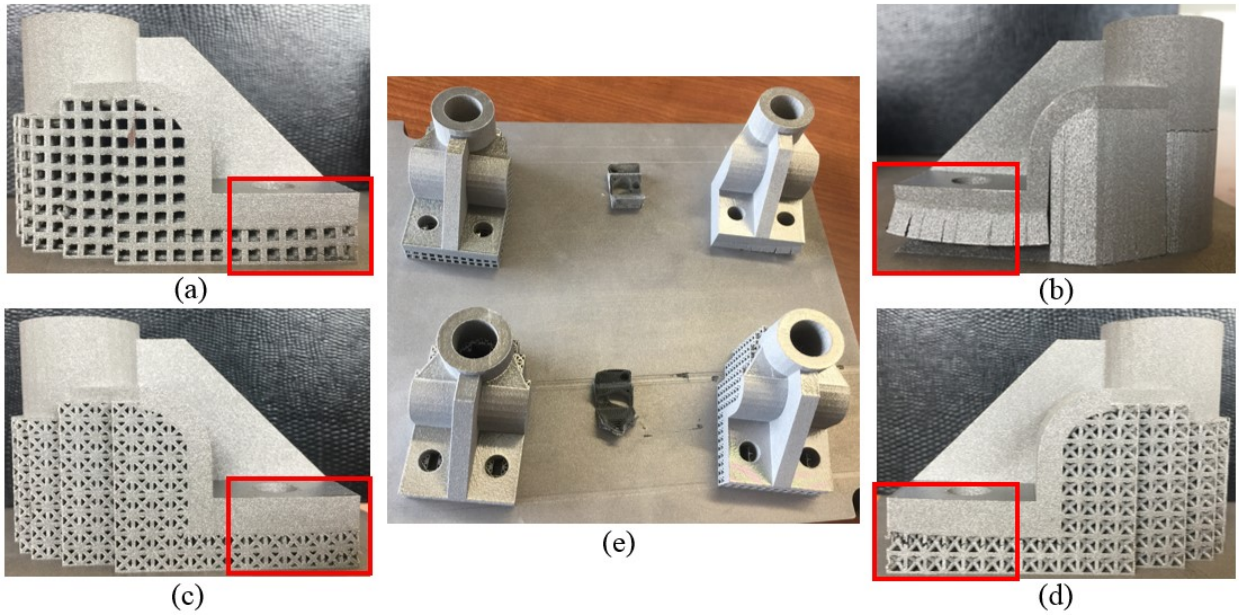

Fig. 21. Printed samples in default orientation with different support structures: (a) side view of the bearing bracket with cubic lattice support structure, (b) side view of the bearing bracket with shell wall support structure, (c) side view of the bearing bracket with cross lattice support structure (d) side view of the bearing bracket with diagonal lattice support structure, (e) front view of the printed bearing bracket. Note that cracks are highlighted by red box in figure (a-d).

The following task is to apply the proposed method to find an optimal orientation for the bearing bracket based on different lattice structure supports. The first test is the cubic lattice structure, whose geometry is given in Fig. 12 (a). The material properties obtained from the homogenized model for elasticity and multiscale model for plasticity are applied to the support voxels in the analysis to calculate the maximum residual stress. The initial distribution of the maximum residual stress is plotted in Fig. 22(a) and 22(b), respectively. It can be observed that the distribution is much difference from the support volume distribution given in Fig. 18(a). This implies that there is a trade-off between support volume minimization and maximum residual stress minimization. Figure 22(c) presents the convergence history of the optimization. The minimum value of the maximum normalized stress converges from 1.56 to 1.06 after 54 iterations with a reduction of 32.1%, while the bearing bracket is orientated at (θ,ϕ)=(-2.359, 0.08). The corresponding support volume in this orientation is 1.0212×10^4 mm^4, which is 3.224×10^3 mm^4 larger than the result of support volume optimization. The voxel-based mesh and the normalized stress distribution of the optimal design are given Fig. 22(d) and (e), respectively, while the realization of the support structure using cubic lattice structure is provided in Fig. 22(f) including the bottom view of the support. Compared with the optimal support volume in Fig. 18(d), the cylindrical feature is rotated to the downward direction of the building direction and the part deviates a little along the build direction (i.e. $\varphi = 0.08$). The bottom view also illustrates this observation. Another interesting observation is that the optimization tends to orient the part with edge overhangs. This implies that edge overhang for cubic lattice structure may have smaller residual stress.

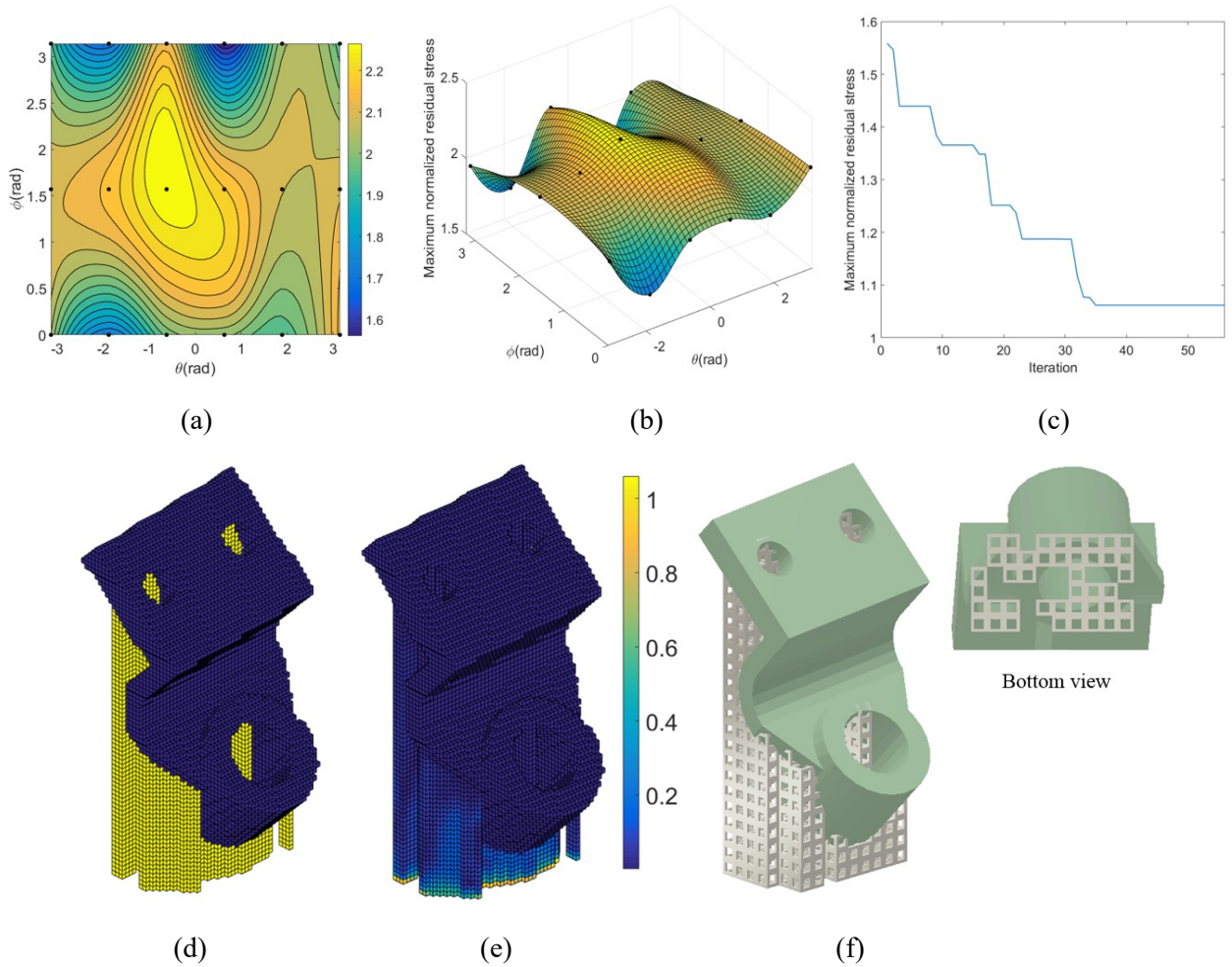

Fig. 22. Orientation optimization of maximum residual stress minimization for bearing bracket with cubic lattice structure support: (a) contour plot of the initially maximum normalized stress distribution; (b) surface plot of the initially maximum normalized stress distribution; (c) convergence history of the objective function; (d) and (e) optimal orientation and the corresponding normalized stress distribution; (f) optimal orientation design reconstructed by cubic lattice structure.

The second test lattice structure is the diagonal lattice structure, whose geometry is given in Fig. 12(b). The optimization results for support structure consisting of diagonal lattice structure are illustrated in Fig. 23. Due to the change of the lattice geometry, the initially maximum residual stress distribution in Fig. 23(a) and (b) is different from the case of cubic lattice structure in Fig. 22(a) and (b), but the regions are much similar. The convergence history of the best objective function in each iteration is shown in Fig. 23(c). After 50 iterations, the best maximum normalized residual stress is reduced from 1.24 to 0.93, which is below the yield strength and a reduction of 25% after optimization. The bearing bracket is oriented in the direction (θ, ϕ)=(-2.343, 0.004) and the support volume is 3.288×10^4 mm^3. Due to the existence of the internal ligaments in the diagonal lattice structure, the optimal orientation and support volume are different from cubic lattice structure. The voxel-based mesh, normalized stress distribution and reconstruction for support structure design by diagonal lattice structure are given in Fig. 23 (d-f), respectively. From the bottom view of reconstruction, the part is more straightforward compared with the cubic design (i.e. $\varphi = 0.004$).

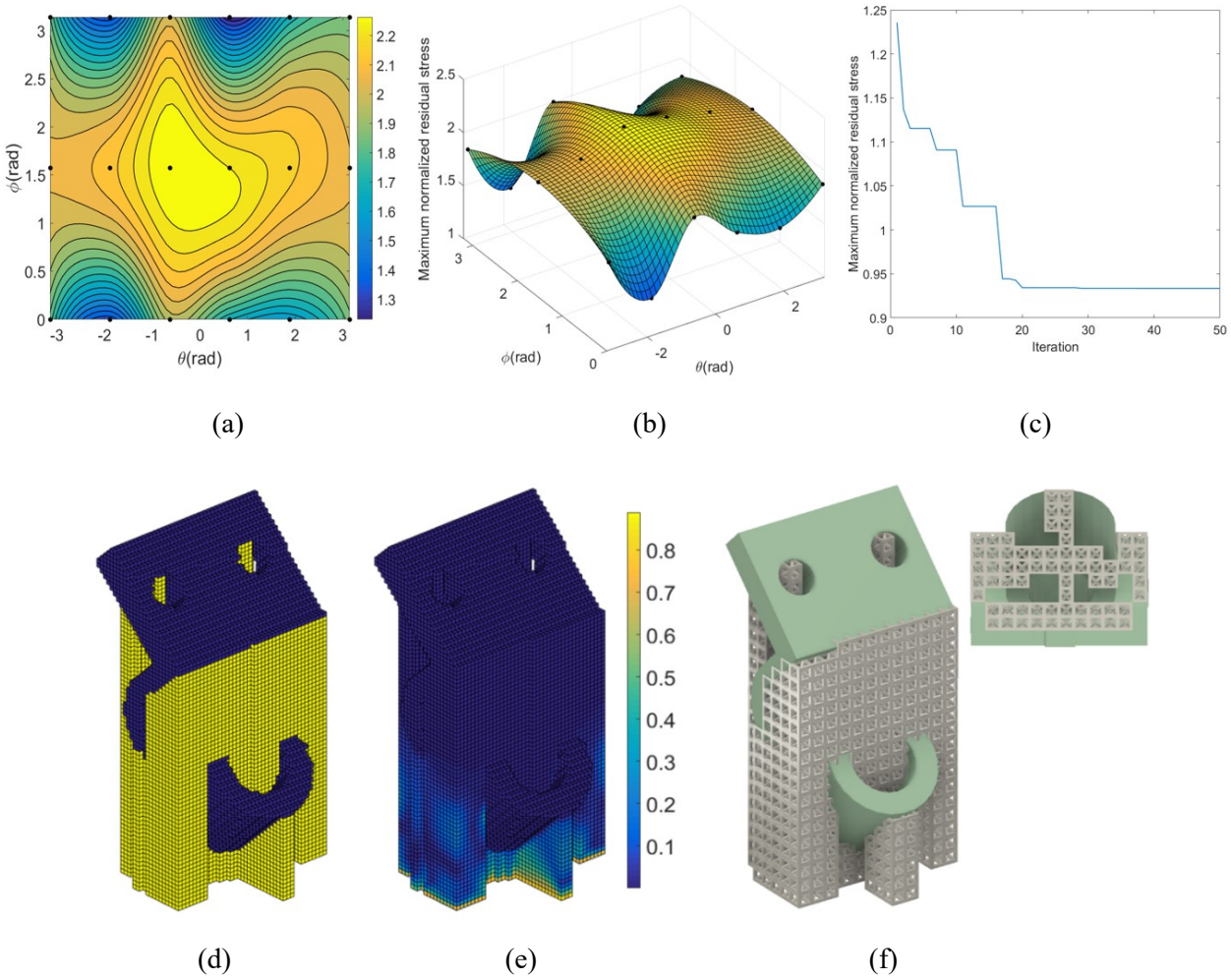

Fig. 23. Orientation optimization of maximum residual stress minimization for bearing bracket with diagonal lattice structure support: (a) contour plot of the initially maximum normalized stress distribution; (b) surface plot of the initially maximum normalized stress distribution; (c) convergence history of the objective function; (d) and (e) optimal orientation and the corresponding normalized stress distribution; (f) optimal orientation design reconstructed by diagonal lattice structure.

Again, the stress optimization is conducted on the build with support structure consisted of the cross-lattice structure. Compared with cubic lattice structure, twelve ligaments are added to the six faces of the cubic lattice structure, refer to Fig. 12 (c). The optimization results are illustrated in Fig. 24. The objective function converges from 1.48 to 1.16 after 37 iterations and the bracket is oriented in the direction (θ, ϕ)=(2.348, 0). The support volume at the optimal orientation is 3.007×10^4 mm^3. For comparison purpose, the optimization results of the three lattice structures are tabulated in Table 1. Based on the comparison, it can be concluded that the geometry of the lattice structure has a significant influence on the stress optimization, in which the diagonal lattice structure exhibits the best performance among the three lattice structures. By rotating the component, the maximum residual stress can be considerably reduced, but cannot guarantee the magnitude of the maximum stress is less than the yield strength. Moreover, the computational cost per orientation and the total cost are also tabulated in Table 1. It can be observed that the simulation time per orientation is 20.9 s while the total optimization cost varies with the change of lattice structure. Differentiating from the support volume minimization, stress analysis is much more time-

consuming than the volume calculation due to the process of FCM analysis for residual stresses. The general computation cost of build orientation for bearing bracket is 3-5 hours using the in-house code. The computation cost should be acceptable to practicing designers and operators as typical complex parts take days to build by powder bed process. To further accelerate the optimization, potential improvement can be achieved in the future by implementing the proposed method using a GPU-based platform.

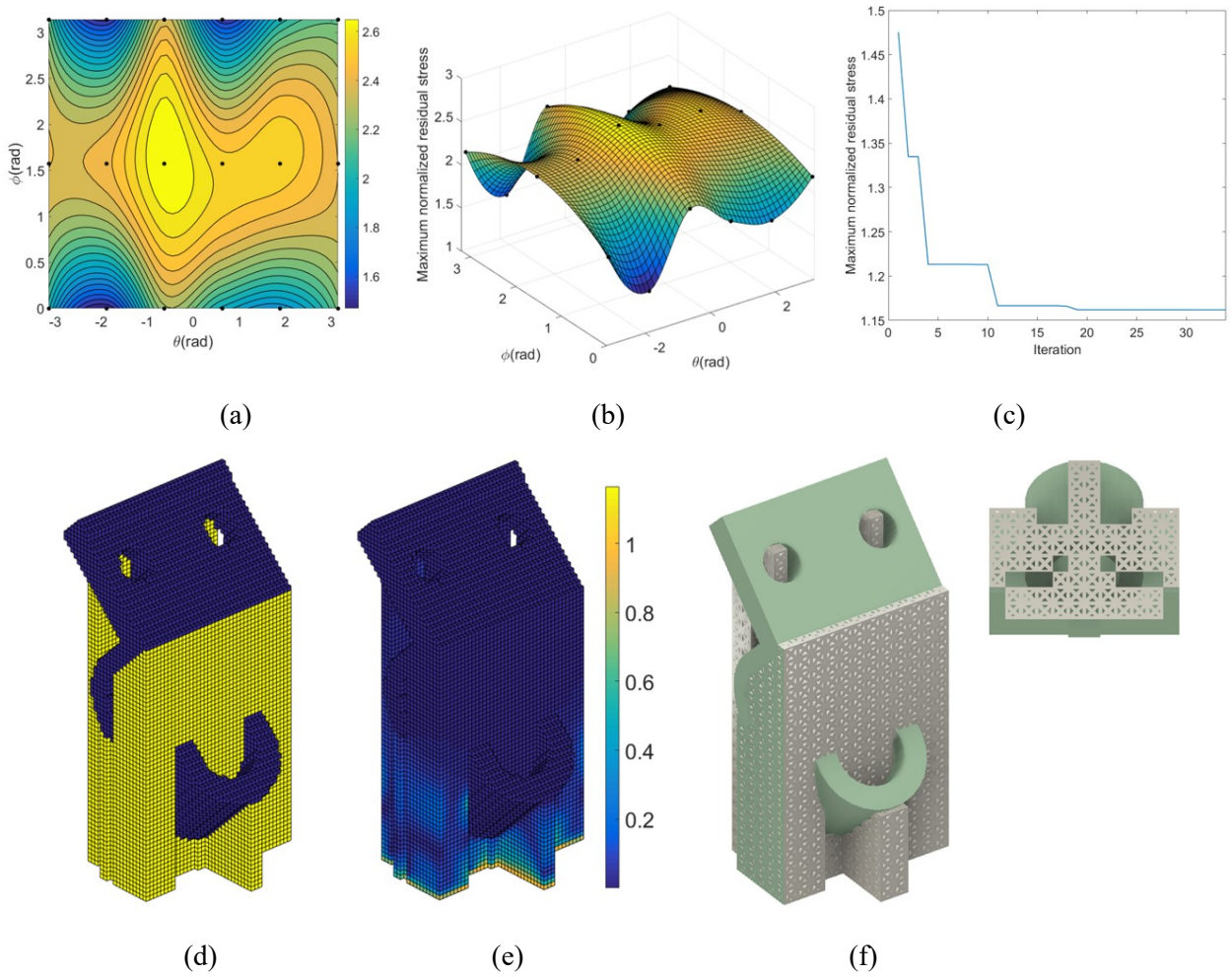

Fig. 24. Orientation optimization of maximum residual stress minimization for bearing bracket with cross lattice structure support. (a) contour plot of the initially maximum stress distribution; (b) surface plot of the initially maximum stress distribution; (c) convergence history of the objective function; (d) and (e) Optimal orientation and the corresponding normalized stress distribution; (f) optimal orientation design reconstructed by cross lattice structure.

Table 1 Comparison of the optimization results of the three lattice structure types

	Cubic	Diagonal	Cross
Initially smallest maximum normalized stress	1.56	1.24	1.48
Optimized maximum normalized stress	1.06	0.93	1.16
Optimal orientation (ϕ, φ)	(-2.359, 0.08)	(-2.343, 0.004)	(2.348, 0)
Support volume of optimal orientation (mm^3)	1.0212×10^4	3.288×10^4	3.007×10^4
Total Iteration	54	50	37

Average computational cost per orientation (seconds)	20.9		
Total computational cost (hours)	5.62	5.21	3.85

To examine the performance of the proposed methodology, the three designs shown in Fig. 22(f), Fig. 23(f) and Fig. 24(f) are printed out in Ti6Al4V using the EOS DMLS system. Compared with the samples shown in Fig. 21, it can be observed in Fig. 25 that all the three designs are successfully printed out without obvious deformation. This implies that although the maximum residual stress is larger than yield strength for cubic and cross lattice supports, the components can still be printed out successfully without obvious cracks. The photos also prove that the overhang detection and support structure generation are efficient for a given component.

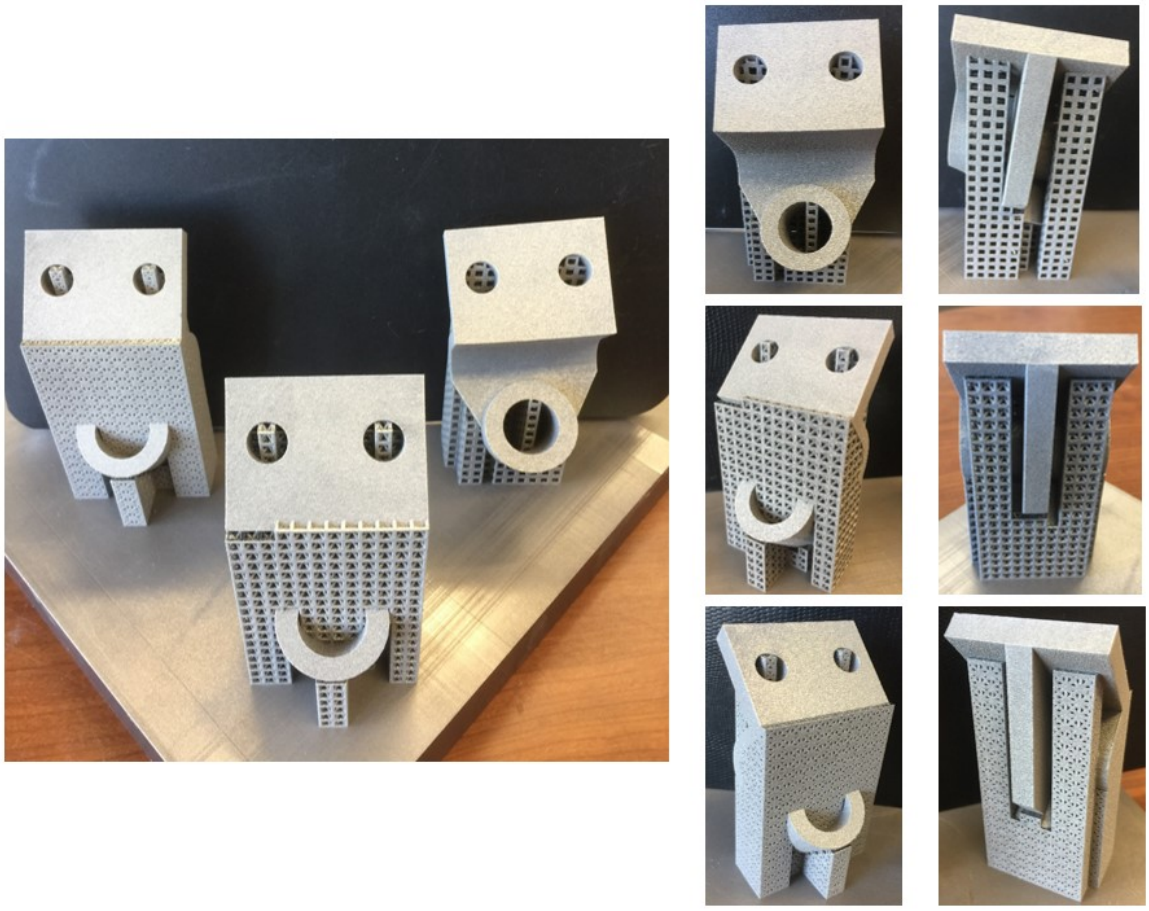

Fig. 25. Photos of the printed-out bearing bracket with support structure consisted of three lattice structures.

5.3 Study of Multi-objective Optimization

In the previous two sections, a single objective function was developed to find a build orientation to minimize support volume or maximum residual stress. Minimizing both the support volume and maximum residual stress simultaneously may be more important for practical applications, since support structure as a sacrificial structure is removed after the manufacturing. To compare with the previous results, the same bearing bracket is employed, and different weight factor, such as 0, 0.2, 0.4, 0.6, 0.8 and 1.0, in Eq. (1) is

investigated. Note that diagonal lattice structure is used as the support material due to its good performance for stress minimization, and the volume fraction is set to be 0.3. There are eighteen particles initially distributed in the design domain. The PSO method [55] is employed to conduct the optimization to minimize the two objectives together.

The convergence history of the simultaneous optimization of support volume and maximum residual stress for different weight factors are illustrated in Fig. 26. Table 2 tabulates the corresponding optimal values of the objectives and design variables. Both of the two objectives oscillate remarkably in the first 30 iterations and then converge to the optimal results. By comparing the two objectives with respect to a weight factor, it can be observed that as the weight factor is increased from 0 to 1, the maximum normalized residual stress increases from 0.9334 to 1.31, while the minimum support volume decreases from $3.29 \times 10^4 \text{mm}^3$ to 6.83×10^3 mm^3. Especially, when $w = 0.4$ and $w = 0.6$, the support volume is on the same order as the minimum value, while the maximum residual stress is in the safe zone (i.e. less than yield strength). This implies that it is possible to orient a given component with prescribed lattice support to minimize the support volume, and at the same time ensure its manufacturability by minimizing the maximum residual stress below the material's yield strength.

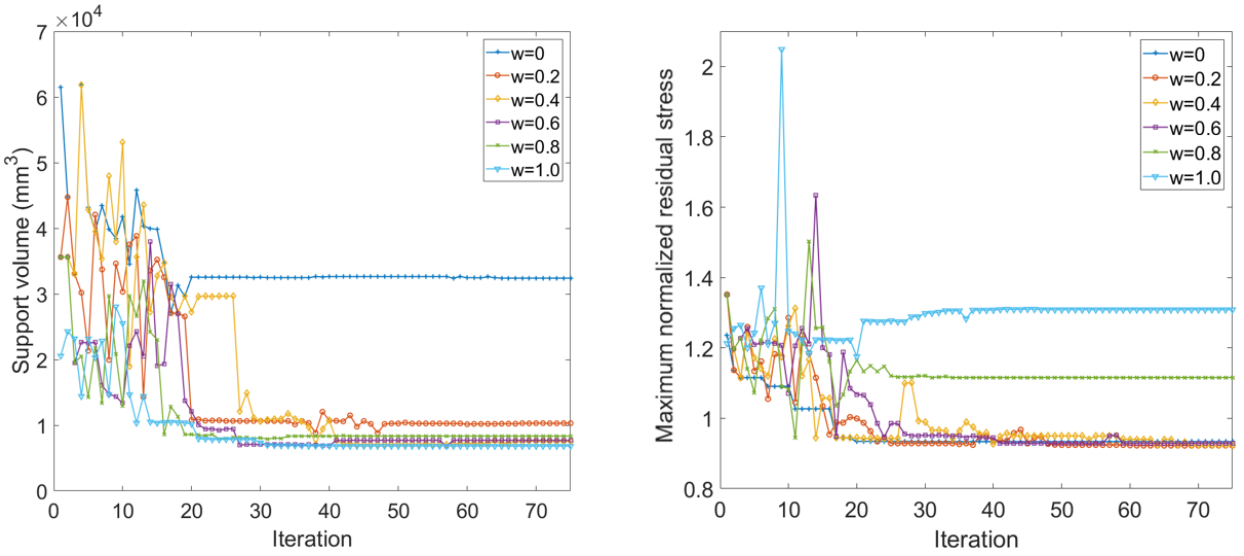

(a) (b)

Fig. 26. Multi-objective optimization results for bearing bracket by considering both the minimum of support volume and the maximum residual stress with different weight factors. (a) Results of support volume; (b) Result of maximum normalized residual stress.

Table 2 Comparison of the optimal results for different weight factors

	$w = 0$	$w = 0.2$	$w = 0.4$	$w = 0.6$	$w = 0.8$	$w = 1.0$
Optimal support volume (mm^3)	3.29×10^4	1.03×10^4	7.51×10^3	7.70×10^3	8.45×10^3	6.83×10^3
Maximum normalized residual stress	0.9334	0.9504	0.9546	0.9450	1.11	1.31
Optimal Orientation	$\theta = -2.343$ $\varphi = 0.004$	$\theta = -2.352$ $\varphi = 0.151$	$\theta = -2.372$ $\varphi = 0.187$	$\theta = 0.771$, $\varphi = 2.954$	$\theta = -2.365$ $\varphi = 2.975$	$\theta = -2.356$ $\varphi = 3.130$

Figure 27 illustrates the build orientation of the bearing bracket after optimization using different weight factors. As the weight factor is increased from 0 to 1, and the weight of the stress objective becomes less important, the cylindrical feature is gradually rotated upward to achieve the minimum support volume. It is also proved that the orientation of the component plays an important role in the build of the component, especially the manufacturability for metal AM components. Figure 28 illustrates the normalized stress distribution with respect to the six build orientations shown in Fig. 27. It can be observed that, when $w \leq 0.6$, the maximum normalized residual stress of the four optimal orientations is at the same level (e.g. 0.93~0.95), while for $w > 0.6$, the maximum normalized stress is larger than the yield strength (e.g. 1.1~1.3) and larger stresses are mainly distributed in the support structures under the edge overhang.

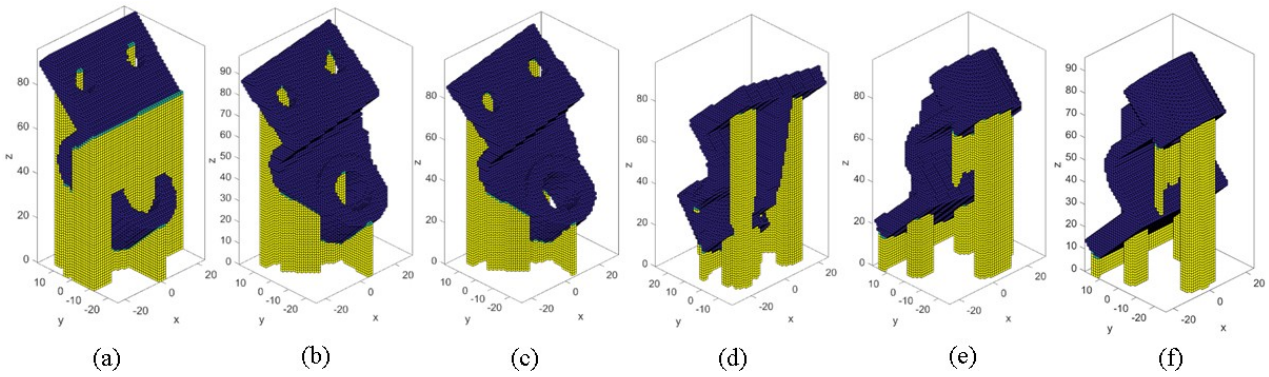

Fig. 27. Optimal results for bear bracket with different weight factor. (a) Voxel-based design for $w = 0$; (b) Voxel-based design for $w = 0.2$; (c) Voxel-based design for $w = 0.4$; (d) Voxel-based design for $w = 0.6$; (e) Voxel-based design for $w = 0.8$; (f) Voxel-based design for $w = 1.0$.

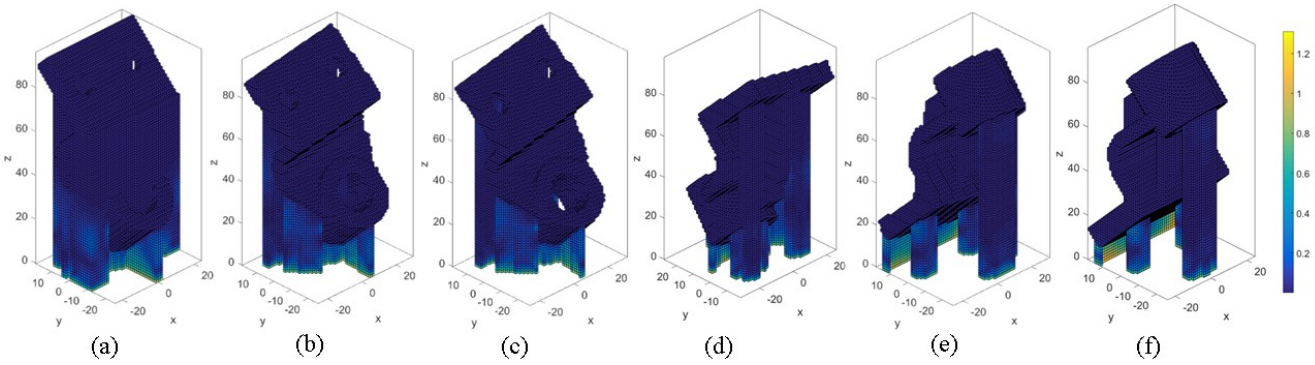

Fig. 28. Normalized residual stress results for bear bracket with different weight factor. (a) Voxel-based design for $w = 0$; (b) Voxel-based design for $w = 0.2$; (c) Voxel-based design for $w = 0.4$; (d) Voxel-based design for $w = 0.6$; (e) Voxel-based design for $w = 0.8$; (f) Voxel-based design for $w = 1.0$.

6. Conclusion

In this work, a novel multi-objective optimization framework is proposed to automatically determine the optimal build orientation for complex components to minimize the support volume and maximum residual stress. First, a voxel-based methodology is employed to generate efficient Cartesian mesh for both bulk component and its support structure for FEA. Differentiating from previous works, a new overhang categorization scheme is developed to divide overhang voxels into three groups: Facet overhang, edge overhang, and point overhang. A benchmark is designed to illustrate the efficiency of the new voxel-based support generation method. Instead of using the default support structure from the Magics software, cubic

lattice structures, such as simple cubic lattice structure, diagonal lattice structure and cross lattice structure, are used to investigate the influence of the lattice structure type on the orientation optimization. Due to its self-supporting and open-cell nature, lattice structure is an ideal structure for support structure design. The AH method and a multiscale model are employed to compute both the effective elastic and plastic properties. This avoids expensive computational cost to implementation of lattice structure for FEA. Second, the inherent strain method is used to efficiently perform analysis to compute the residual stress for the component printed by powder bed metal AM. To avoid the mesh generation in the optimization iterations, the voxel-based Cartesian mesh is used to discretize the design domain of a given component and solve the problem. The fictitious domain method (i.e. finite cell method) is used to conduct the analysis. Finally, a multi-objective optimization framework is proposed to find the optimal build orientation for a component with minimum support volume and/or maximum residual stress. Several numerical examples are studied to examine the performance of the optimization. First, we compare the new method with previous methods for support volume minimization. Second, the single objective of minimizing the maximum residual stress is performed for the realistic component with three different types of lattice structures. It is found that the geometry of lattice structure plays an important role in the optimal orientation for stress minimization. The diagonal lattice structure exhibits the best performance among the lattices that also include simple cubic lattice structure and cross lattice structure. In particular, the three designs are successfully printed out, which further demonstrate the efficiency of the proposed method. Third, multi-objective optimization for support volume and weight is conducted to the same component. It is observed that it is possible to achieve minimization of support volume while limiting the maximum residual stress under yield strength by selecting appropriate lattice structure.

Note that although the proposed methodology can ensure manufacturability of AM builds, the removability of the lattice structure support by post-machining has not been considered and will be investigated in our future work. Further studies could be performed to add other constraints to the optimization algorithm by considering area of the surface that is not accessible by post-machining. Another alternative to remove support structure is by using dissolvable support [57, 58], which is a self-terminating chemical process that dissolves a thin surface layer. Hence, if the struts or walls in the lattice support are made thin enough, the support structure can be dissolved using this chemical process without any post-machining. These topics will be investigated in future in order to completely solve the build failure and post support removal for the powder bed fusion process.

Acknowledgements

The authors would like to acknowledge the support from the National Science Foundation (CMMI-1634261).

Reference

[1] L. Cheng, X. Liang, E. Belski, X. Wang, J. M. Sietins, S. Ludwick*, et al.*, "Natural Frequency Optimization of Variable-Density Additive Manufactured Lattice Structure: Theory and Experimental Validation," *Journal of Manufacturing Science and Engineering,* vol. 140, p. 105002, 2018.

[2] P. Mercelis and J.-P. Kruth, "Residual stresses in selective laser sintering and selective laser melting," *Rapid Prototyping Journal,* vol. 12, pp. 254-265, 2006.

[3] J.-P. Kruth, L. Froyen, J. Van Vaerenbergh, P. Mercelis, M. Rombouts, and B. Lauwers, "Selective laser melting of iron-based powder," *Journal of Materials Processing Technology,* vol. 149, pp. 616-622, 2004.

[4] L. Papadakis, A. Loizou, J. Risse, and J. Schrage, "Numerical computation of component shape distortion manufactured by selective laser melting," *Procedia CIRP,* vol. 18, pp. 90-95, 2014.

[5] S. Leuders, M. Thöne, A. Riemer, T. Niendorf, T. Tröster, H. Richard*, et al.*, "On the mechanical behaviour of titanium alloy TiAl6V4 manufactured by selective laser melting: Fatigue resistance and crack growth performance," *International Journal of Fatigue,* vol. 48, pp. 300-307, 2013.

[6] E. O. t. Olakanmi, R. Cochrane, and K. Dalgarno, "A review on selective laser sintering/melting (SLS/SLM) of aluminium alloy powders: Processing, microstructure, and properties," *Progress in Materials Science,* vol. 74, pp. 401-477, 2015.

[7] S. Allen and D. Dutta, "On the computation of part orientation using support structures in layered manufacturing," in *Proceedings of Solid Freeform Fabrication Symposium, University of Texas at Austin, Austin, TX, June*, 1994, pp. 259-269.

[8] D. Frank and G. Fadel, "Expert system-based selection of the preferred direction of build for rapid prototyping processes," *Journal of Intelligent Manufacturing,* vol. 6, pp. 339-345, 1995.

[9] Y. Cai, L. Xu, and G. Cheng, "Novel numerical implementation of asymptotic homogenization method for periodic plate structures," *International Journal of Solids and Structures,* vol. 51, pp. 284-292, 2014/01/01/ 2014.

[10] M. P. Bendsøe and O. Sigmund, "Material interpolation schemes in topology optimization," *Archive of applied mechanics,* vol. 69, pp. 635-654, 1999.

[11] W. Zhang and S. Sun, "Scale-related topology optimization of cellular materials and structures," *International journal for numerical methods in engineering,* vol. 68, pp. 993-1011, 2006.

[12] K. Tantikom, T. Aizawa, and T. Mukai, "Symmetric and asymmetric deformation transition in the regularly cell-structured materials. Part I: experimental study," *International Journal of Solids and Structures,* vol. 42, pp. 2199-2210, 2005/04/01/ 2005.

[13] K. Thrimurthulu, P. M. Pandey, and N. V. Reddy, "Optimum part deposition orientation in fused deposition modeling," *International Journal of Machine Tools and Manufacture,* vol. 44, pp. 585-594, 2004.

[14] K. Mumtaz, P. Vora, and N. Hopkinson, "A method to eliminate anchors/supports from directly laser melted metal powder bed processes," in *Proc. Solid Freeform Fabrication Symposium*, 2011, pp. 55-64.

[15] G. Strano, L. Hao, R. Everson, and K. Evans, "A new approach to the design and optimisation of support structures in additive manufacturing," *The International Journal of Advanced Manufacturing Technology,* vol. 66, pp. 1247-1254, 2013.

[16] A. Hussein, L. Hao, C. Yan, R. Everson, and P. Young, "Advanced lattice support structures for metal additive manufacturing," *Journal of Materials Processing Technology,* vol. 213, pp. 1019-1026, 2013.

[17] F. Calignano, "Design optimization of supports for overhanging structures in aluminum and titanium alloys by selective laser melting," *Materials & Design,* vol. 64, pp. 203-213, 2014.

[18] R. Vaidya and S. Anand, "Optimum Support Structure Generation for Additive Manufacturing Using Unit Cell Structures and Support Removal Constraint," *Procedia Manufacturing,* vol. 5, pp. 1043-1059, 2016.

[19] R. Paul and S. Anand, "Optimization of layered manufacturing process for reducing form errors with minimal support structures," *Journal of Manufacturing Systems,* vol. 36, pp. 231-243, 2015.
[20] P. Das, K. Mhapsekar, S. Chowdhury, R. Samant, and S. Anand, "Selection of build orientation for optimal support structures and minimum part errors in additive manufacturing," *Computer-Aided Design and Applications,* pp. 1-13, 2017.
[21] P. Das, R. Chandran, R. Samant, and S. Anand, "Optimum part build orientation in additive manufacturing for minimizing part errors and support structures," *Procedia Manufacturing,* vol. 1, pp. 343-354, 2015.
[22] X. Zhang, X. Le, A. Panotopoulou, E. Whiting, and C. C. Wang, "Perceptual models of preference in 3D printing direction," *ACM Transactions on Graphics (TOG),* vol. 34, p. 215, 2015.
[23] M. Ruess, D. Tal, N. Trabelsi, Z. Yosibash, and E. Rank, "The finite cell method for bone simulations: verification and validation," *Biomechanics and modeling in mechanobiology,* vol. 11, pp. 425-437, 2012.
[24] D. Schillinger, A. Düster, and E. Rank, "The hp-d-adaptive finite cell method for geometrically nonlinear problems of solid mechanics," *International Journal for Numerical Methods in Engineering,* vol. 89, pp. 1171-1202, 2012.
[25] A. Düster, J. Parvizian, Z. Yang, and E. Rank, "The finite cell method for three-dimensional problems of solid mechanics," *Computer methods in applied mechanics and engineering,* vol. 197, pp. 3768-3782, 2008.
[26] J. Parvizian, A. Düster, and E. Rank, "Finite cell method," *Computational Mechanics,* vol. 41, pp. 121-133, 2007.
[27] S. Ly, A. M. Rubenchik, S. A. Khairallah, G. Guss, and M. J. Matthews, "Metal vapor micro-jet controls material redistribution in laser powder bed fusion additive manufacturing," *Scientific reports,* vol. 7, p. 4085, 2017.
[28] X. Liang, L. Cheng, Q. Chen, Q. Yang, and A. C. To, "A modified method for estimating inherent strains from detailed process simulation for fast residual distortion prediction of single-walled structures fabricated by directed energy deposition," *Additive Manufacturing,* vol. 23, pp. 471-486, 2018/10/01/ 2018.
[29] M. Bugatti and Q. Semeraro, "Limitations of the inherent strain method in simulating powder bed fusion processes," *Additive Manufacturing,* vol. 23, pp. 329-346, 2018/10/01/ 2018.
[30] B. Ahmad, S. O. van der Veen, M. E. Fitzpatrick, and H. Guo, "Residual stress evaluation in selective-laser-melting additively manufactured titanium (Ti-6Al-4V) and inconel 718 using the contour method and numerical simulation," *Additive Manufacturing,* vol. 22, pp. 571-582, 2018/08/01/ 2018.
[31] L. Cheng, J. Bai, and A. C. To, "Functionally graded lattice structure topology optimization for the design of additive manufactured components with stress constraints," *Computer Methods in Applied Mechanics and Engineering,* vol. 344, pp. 334-359, 2019/02/01/ 2019.
[32] Z. Yan, F. Zhang, J. Wang, F. Liu, X. Guo, K. Nan*, et al.*, "Controlled mechanical buckling for origami-inspired construction of 3D microstructures in advanced materials," *Advanced functional materials,* vol. 26, pp. 2629-2639, 2016.
[33] O. Poyraz, E. Yasa, G. Akbulut, A. Orhangul, and S. Pilatin, "Investigation of support structures for direct metal laser sintering (DMLS) of IN625 parts," in *Proceedings of Solid Freeform Fabrication (SFF) Symposium, Austin, TX, USA*, 2015.
[34] J. Vanek, J. A. Galicia, and B. Benes, "Clever support: Efficient support structure generation for digital fabrication," in *Computer Graphics Forum*, 2014, pp. 117-125.
[35] M. Schwarz and H.-P. Seidel, "Fast parallel surface and solid voxelization on GPUs," in *ACM Transactions on Graphics (TOG)*, 2010, p. 179.
[36] Z. Dong, W. Chen, H. Bao, H. Zhang, and Q. Peng, "Real-time voxelization for complex polygonal models," in *Computer Graphics and Applications, 2004. PG 2004. Proceedings. 12th Pacific Conference on*, 2004, pp. 43-50.

[37] B. Hassani and E. Hinton, "A review of homogenization and topology optimization I—homogenization theory for media with periodic structure," *Computers & Structures,* vol. 69, pp. 707-717, 1998.
[38] S. J. Hollister and N. Kikuchi, "A comparison of homogenization and standard mechanics analyses for periodic porous composites," *Computational Mechanics,* vol. 10, pp. 73-95, 1992.
[39] A. E. Patterson, S. L. Messimer, and P. A. Farrington, "Overhanging Features and the SLM/DMLS Residual Stresses Problem: Review and Future Research Need," *Technologies,* vol. 5, p. 15, 2017.
[40] C. Li, C. Fu, Y. Guo, and F. Fang, "Fast prediction and validation of part distortion in selective laser melting," *Procedia Manufacturing,* vol. 1, pp. 355-365, 2015.
[41] Q. Yang, P. Zhang, L. Cheng, Z. Min, M. Chyu, and A. C. To, "Finite element modeling and validation of thermomechanical behavior of Ti-6Al-4V in directed energy deposition additive manufacturing," *Additive Manufacturing,* vol. 12, pp. 169-177, 2016.
[42] W. Yan, S. Lin, O. L. Kafka, Y. Lian, C. Yu, Z. Liu*, et al.*, "Data-driven multi-scale multi-physics models to derive process–structure–property relationships for additive manufacturing," *Computational Mechanics,* pp. 1-21, 2018.
[43] B. Schoinochoritis, D. Chantzis, and K. Salonitis, "Simulation of metallic powder bed additive manufacturing processes with the finite element method: A critical review," *Proceedings of the Institution of Mechanical Engineers, Part B: Journal of Engineering Manufacture,* vol. 231, pp. 96-117, 2017.
[44] M. Masoomi, S. M. Thompson, and N. Shamsaei, "Laser powder bed fusion of Ti-6Al-4V parts: Thermal modeling and mechanical implications," *International Journal of Machine Tools and Manufacture,* vol. 118-119, pp. 73-90, 2017/08/01/ 2017.
[45] S. Shrestha and K. Chou, "A build surface study of Powder-Bed Electron Beam Additive Manufacturing by 3D thermo-fluid simulation and white-light interferometry," *International Journal of Machine Tools and Manufacture,* vol. 121, pp. 37-49, 2017/10/01/ 2017.
[46] N. Keller and V. Ploshikhin, "New method for fast predictions of residual stress and distortion of AM parts."
[47] X. Liang, Q. Chen, L. Cheng, Q. Yang, and A. To, "A modified inherent strain method for fast prediction of residual deformation in additive manufacturing of metal parts."
[48] I. Setien, M. Chiumenti, S. van der Veen, M. San Sebastian, F. Garciandía, and A. Echeverría, "Empirical methodology to determine inherent strains in additive manufacturing," *Computers & Mathematics with Applications,* 2018.
[49] M. Siewert, F. Neugebauer, J. Epp, and V. Ploshikhin, "Validation of Mechanical Layer Equivalent Method for simulation of residual stresses in additive manufactured components," *Computers & Mathematics with Applications,* 2018/10/09/ 2018.
[50] R. Glowinski and Y. Kuznetsov, "Distributed Lagrange multipliers based on fictitious domain method for second order elliptic problems," *Computer Methods in Applied Mechanics and Engineering,* vol. 196, pp. 1498-1506, 2007.
[51] T. Yamada, K. Izui, S. Nishiwaki, and A. Takezawa, "A topology optimization method based on the level set method incorporating a fictitious interface energy," *Computer Methods in Applied Mechanics and Engineering,* vol. 199, pp. 2876-2891, 2010.
[52] I. Ramiere, P. Angot, and M. Belliard, "A fictitious domain approach with spread interface for elliptic problems with general boundary conditions," *Computer Methods in Applied Mechanics and Engineering,* vol. 196, pp. 766-781, 2007.
[53] Q. Cai, S. Kollmannsberger, R.-P. Mundani, and E. Rank, "The finite cell method for solute transport problems in porous media," in *Proceedings of the international conference on finite elements in flow problems*, 2011.
[54] Z. Yang, M. Ruess, S. Kollmannsberger, A. Düster, and E. Rank, "An efficient integration technique for the voxel-based finite cell method," *International Journal for Numerical Methods in Engineering,* vol. 91, pp. 457-471, 2012.

[55] J. Kennedy, "Particle swarm optimization," in *Encyclopedia of machine learning*, ed: Springer, 2011, pp. 760-766.
[56] I. Y. Kim and O. L. de Weck, "Adaptive weighted-sum method for bi-objective optimization: Pareto front generation," *Structural and multidisciplinary optimization,* vol. 29, pp. 149-158, 2005.
[57] C. S. Lefky, B. Zucker, D. Wright, A. R. Nassar, T. W. Simpson, and O. J. Hildreth, "Dissolvable supports in powder bed fusion-printed stainless steel," *3D Printing and Additive Manufacturing,* vol. 4, pp. 3-11, 2017.
[58] O. J. Hildreth, A. R. Nassar, K. R. Chasse, and T. W. Simpson, "Dissolvable metal supports for 3D direct metal printing," *3D Printing and Additive Manufacturing,* vol. 3, pp. 90-97, 2016.

Appendix A

1. Effectively Elastic Properties of Lattice Material

AH method relies on an asymptotic expansion, which assumes that any field quantities (i.e. displacement) can be formulated by quantities as a separation of scales as follows:

$$\boldsymbol{u}^{\epsilon}(\boldsymbol{x},\boldsymbol{y}) = \boldsymbol{u}_0(\boldsymbol{x},\boldsymbol{y}) + \epsilon\boldsymbol{u}_1(\boldsymbol{x},\boldsymbol{y}) + \epsilon^2\boldsymbol{u}_2(\boldsymbol{x},\boldsymbol{y}) + \cdots \tag{1}$$

where $\boldsymbol{x}$ and $\boldsymbol{y}$ represent coordinate vector of the macroscale and microscale, respectively. $\boldsymbol{u}^{\epsilon}(\boldsymbol{x},\boldsymbol{y})$ denotes the exact value of field quantities, $\boldsymbol{u}_0$is the average value that only varies at macroscopic level, while $\boldsymbol{u}_1, \boldsymbol{u}_2, \cdots$ represent the quantity perturbation at microscale due to the existence of microstructural features. ϵ is an amplification factor used to relate two scales $\boldsymbol{y} = \frac{\boldsymbol{x}}{\epsilon}$, which implies that the field quantities at microscale varies $\frac{1}{\epsilon}$ times faster than the macroscale.

To substitute Eq. (1) into the equilibrium equation, one can obtain the following unit cell problem [38].

$$\int_{V_{RVE}} C_{ijpq}\varepsilon_{ij}^{1}(v)\varepsilon_{pq}^{*}(u)\, dV_{RVE} = -\int_{V_{RVE}} C_{ijkl}\varepsilon_{ij}^{1}(v)\bar{\varepsilon}_{pq}(u)\, dV_{RVE} \tag{2}$$

where V_{RVE} represents the volume of RVE, C_{ijpq} is the locally varies elastic tensor, u denotes displacement while v represents the virtual displacement. ε_{ij}^{1} is the virtually fluctuating strain tensor, $\bar{\varepsilon}_{pq}$ denotes the average strain tensor while $\varepsilon_{pq}^{*}$is the fluctuating strain tensor. By solving the unit cell problem in Eq. (2), one can obtain effective properties of lattice structure and macroscopic stress as:

$$\bar{C}_{ijkl} = \frac{1}{|V_{RVE}|}\int_{V_{RVE}} C_{ijmn}M_{mnkl}dV_{RVE} \tag{3}$$

and

$$\bar{\sigma}_{ij} = \frac{1}{|V_{RVE}|}\int_{V_{RVE}} C_{ijmn}M_{mnkl}dV_{RVE}\,\bar{\varepsilon}_{kl} \tag{4}$$

where $\bar{C}_{ijkl}$ denotes effective elastic tensor while $\bar{\sigma}_{ij}$ is the macroscopic stress, and M_{mnkl} is the local structural tensor, which can be obtained by:

$$M_{ijkl} = \frac{1}{2}\left(\delta_{ik}\delta_{jl} + \delta_{il}\delta_{jk}\right) - \varepsilon_{ij}^{*kl} \tag{5}$$

where δ_{ij} is the Kronecker delta and ε_{ij}^{*kl} is the periodicity of the strain field.

Considering the symmetry of the three lattice structures in Fig. 12, there are three independent elastic constants, and the elastic response can be formulated as:

$$\begin{bmatrix}\bar{\sigma}_{11}\\ \bar{\sigma}_{22}\\ \bar{\sigma}_{33}\\ \bar{\sigma}_{12}\\ \bar{\sigma}_{23}\\ \bar{\sigma}_{31}\end{bmatrix} = \begin{bmatrix}\bar{C}_{11} & \bar{C}_{12} & \bar{C}_{12} & 0 & 0 & 0\\ \bar{C}_{12} & \bar{C}_{11} & \bar{C}_{12} & 0 & 0 & 0\\ \bar{C}_{12} & \bar{C}_{12} & \bar{C}_{11} & 0 & 0 & 0\\ 0 & 0 & 0 & \bar{C}_{44} & 0 & 0\\ 0 & 0 & 0 & 0 & \bar{C}_{44} & 0\\ 0 & 0 & 0 & 0 & 0 & \bar{C}_{44}\end{bmatrix}\begin{bmatrix}\bar{\varepsilon}_{11}\\ \bar{\varepsilon}_{22}\\ \bar{\varepsilon}_{33}\\ 2\bar{\varepsilon}_{12}\\ 2\bar{\varepsilon}_{23}\\ 2\bar{\varepsilon}_{31}\end{bmatrix} \tag{6}$$

where $\bar{C}_{11}, \bar{C}_{12}$ and $\bar{C}_{44}$ represent three independent elastic constants computed from Eq. (3), which are the function of relative density, $\bar{\sigma}_{ij}$ and $\bar{\varepsilon}_{ij}$ $(i,j = 1,2,3)$ are the macroscopic stress and strain, respectively, by solving the governing equation at macroscale using constitutive model in Eq. (3).

2. Anisotropic yield criterion for lattice material

With regard to the stress calculation for lattice structure, a multiscale model proposed in [31] is used to relate macroscopic stress computed from homogenized model to microscale stresses of the lattice structure. The Hill's yield criterion is employed to describe the relationship as:

$$(\bar{\sigma}^H)^2 = A(\bar{\sigma}_{11} - \bar{\sigma}_{22})^2 + B(\bar{\sigma}_{22} - \bar{\sigma}_{33})^2 + C(\bar{\sigma}_{33} - \bar{\sigma}_{11})^2 + 2D\bar{\sigma}_{12}^2 + 2E\bar{\sigma}_{23}^2 + 2F\bar{\sigma}_{13}^2 \quad (7)$$

where $\bar{\sigma}^H$ represents effective Hill's stress on macroscopic level and $\bar{\sigma}_{ij}$ denote effective stress tensor calculated based on the homogenized model from Eq. (10), A, B, C, D, E and F are plastic constants used to capture anisotropy of lattice material. It is noted that these plastic constants are a function of relative density. When the relative density of lattice structure is equal to one, $\bar{\sigma}^H$ is degenerated to von Mises stress; when relative density is less than one, stress in Eq. (11) is used to capture the anisotropy of lattice material.

According to the symmetry of the lattice structure in Fig. 12, the plastic constants can be further reduced to two, i.e. $A = B = C = K$ and $2D = 2E = 2F = Q$, and the in-matrix notation, the Hill's yield criterion can be written as:

$$(\bar{\sigma}^H)^2 = \bar{\boldsymbol{\sigma}}^T \mathbb{M} \bar{\boldsymbol{\sigma}} \quad (8)$$

where $\bar{\boldsymbol{\sigma}} = \{\bar{\sigma}_{11}, \bar{\sigma}_{22}, \bar{\sigma}_{33}, \bar{\sigma}_{12}, \bar{\sigma}_{13}, \bar{\sigma}_{23}\}$ represents macroscopic stress tensor; $\mathbb{M}$ denotes the plastic constants matrix, and can be written as

$$\mathbb{M} = \begin{bmatrix} 2K & -K & -K & 0 & 0 & 0 \\ -K & 2K & -K & 0 & 0 & 0 \\ -K & -K & 2K & 0 & 0 & 0 \\ 0 & 0 & 0 & Q & 0 & 0 \\ 0 & 0 & 0 & 0 & Q & 0 \\ 0 & 0 & 0 & 0 & 0 & Q \end{bmatrix} \quad (9)$$

By using the homogenized model in Eq. (3) and multiscale stress in Eq. (7), full simulation for lattice structure is simplified to analysis of continuum solid material with equivalent elasticity and yield performance. Since lattice structure is not modeled explicitly using very fine mesh, the AH makes it computational less expensive to model lattice structure using voxel-based mesh by assigning homogenized model and yield strength to the support voxel.

Appendix B

1. Implementation of Inherent Strain Method

The implementation of the inherent strain method [28, 30, 49] based on FCM is described schematically in Fig. B1. As illustrated in the figure, the physical domain Ω of powder bed metal AM is consisted of three subdomains: Build tray domain Ω_t, support structure domain Ω_s, and the bulk component domain Ω_c. To simplify the mesh generation, the physical design domain Ω is embedded into a larger domain Ω_e with a boundary of $\partial\Omega_e$. For metal AM, build tray is fixed to a bulk plate to ensure the stability of manufacturing. Thus, a Dirichlet boundary condition of $\boldsymbol{u} = 0$ is subjected to the bottom surface of the build tray. Due to

the coincidence of bottom of build tray and extended domain Ω_e, the fixed boundary condition is directly extended to the bottom voxels in Ω_e.

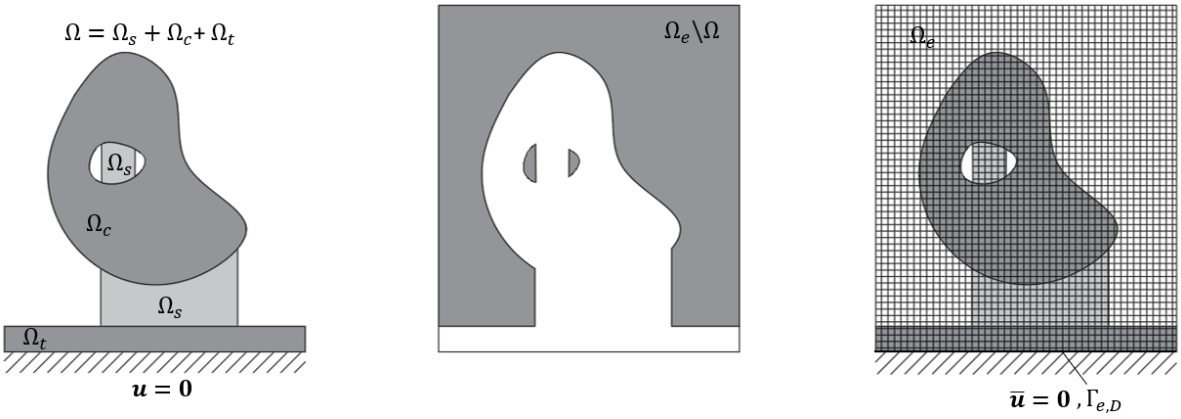

(a) (b) (c)

Fig. B1. The domain Ω in powder bed AM is embedded in voxel-based domain Ω_e. (a) Domain of printed component, which is combination of three subdomains: bulk component domain Ω_c, support structure domain Ω_s, and build tray domain Ω_t; (b) Fictitious domain, and (c) Embedding domain Ω_e.

Based on the works of [25, 26], the weak form of equilibrium equation in the extended domain Ω_e can be formulated as:

$$a_e(\boldsymbol{u}, \boldsymbol{v}) = b_e(\boldsymbol{v}) \tag{10}$$

with the boundary condition of

$$\bar{\boldsymbol{u}} = 0, on\ \Gamma_{e,D} \tag{11}$$

where $\boldsymbol{u}$ and $\boldsymbol{v}$ represent the displacement and test function, respectively. $\Gamma_{e,D}$ is the Dirichlet boundary in the extended domain. The bilinear form is

$$a_e(\boldsymbol{u}, \boldsymbol{v}) = \int_{\Omega_e} [\boldsymbol{B}\boldsymbol{v}]^T \epsilon \boldsymbol{D} [\boldsymbol{B}\boldsymbol{u}]\, d\Omega \tag{12}$$

where $\boldsymbol{B}$ represents the strain-displacement operator, $\boldsymbol{D}$ denotes stiffness matrix, ϵ is a coefficient used to identify physical domain Ω and the fictitious domain $\Omega_e \backslash \Omega$, and its definition is given as:

$$\epsilon(\boldsymbol{x}) = \begin{cases} 1.0 & \forall x \in \Omega \\ 10^{-\mu} & \forall x \in \Omega_e \backslash \Omega \end{cases} \tag{13}$$

where μ is a factor used to avoid the singularity of the calculation and is set to be 8 to ensure the robustness of the calculation. In Eq. (12), the constitutive matrix $\boldsymbol{D}$ is the effective properties for both the bulk component and support structure consisting of lattice structure. Homogenized model proposed in Eq. (3) is used for the material interpolation as

$$\boldsymbol{D} = \bar{\boldsymbol{D}}(\rho) \tag{14}$$

where $\bar{\boldsymbol{D}}(\rho)$ is the constitutive model computed by asymptotic homogenization with ρ denoting the relative density of lattice structure. When $\rho = 1$, the constitutive model is equal to the model of solid material $\boldsymbol{D} = \boldsymbol{C}^*$; when $0 < \rho < 1$, the constitutive model is the model of lattice structure. Since the homogenization is

effective for $\rho \in [0,1]$, the material interpolation for calculation is unified into a single expression and the bilinear form can be written as:

$$a_e(\boldsymbol{u}, \boldsymbol{v}) = \int_{\Omega_e} [\boldsymbol{B}\boldsymbol{v}]^T \epsilon \overline{\boldsymbol{C}}(\rho) [\boldsymbol{B}\boldsymbol{u}] \, d\Omega \tag{15}$$

The inherent strain is applied as a volume load, and the linear functional on the right-hand side of Eq. (10) can be expressed as:

$$b_e(\boldsymbol{v}) = \int_{\Omega_e} \boldsymbol{v}^T \epsilon \boldsymbol{f}^{in} \, d\Omega \tag{16}$$

where $\boldsymbol{f}^{in}$ represents the loading obtained from the inherent strain. For three-dimensional problem, the inherent strain assigned on the element can be formulated as

$$\boldsymbol{f}_e^{in} = \int_{\Omega_e} \boldsymbol{B}^T \boldsymbol{D} \boldsymbol{\varepsilon}_e^{in} \, d\Omega_e \tag{17}$$

After discretization, the weak form equilibrium equation in Eq. (12) becomes

$$\mathbf{K}\mathbf{U} = \mathbf{F}^{in} \tag{18}$$

where $\mathbf{U}$ represents vector of displacement, $\mathbf{K}$ and $\mathbf{F}^{in}$ are the global stiffness matrix and global inherent strain load vector, respectively, which can be computed through the assembly of cell matrices as

$$\mathbf{K} = \sum_{i=1}^{n_{c+s+t}} (\boldsymbol{k}_i) = \sum_{i=1}^{n_{c+s+t}} \left(\int_{\Omega_i} \boldsymbol{B}^T \epsilon \boldsymbol{D} \boldsymbol{B} d\Omega \right) \tag{19}$$

and

$$\mathbf{F}^{in} = \sum_{j=1}^{n_{c+s}} \left(\boldsymbol{f}_j^{in} \right) = \sum_{j=1}^{n_{c+s}} \left(\int_{\Omega_j} \boldsymbol{B}^T \epsilon \boldsymbol{C}^* \boldsymbol{\varepsilon}^{in} d\Omega \right) \tag{20}$$

where n_{c+s+t} denotes total number of cell/voxel in the embedded domain including the domain of bulk component, support structure and build tray, n_{c+s} represents total number of cell/voxel in the domain of bulk component and support structure, $\boldsymbol{k}_i$ and $\boldsymbol{f}_i^{in}$ are the cell stiffness matrix and cell inherent strain load, respectively.